

OCCASO V.

Chemical-abundance trends with Galactocentric distance and age[★]

J. Carbajo-Hijarrubia^{1,2,3}, L. Casamiquela^{1,2,3,4}, R. Carrera⁵, L. Balaguer-Núñez^{1,2,3}, C. Jordi^{1,2,3}, F. Anders^{1,2,3},
C. Gallart^{6,7}, E. Pancino⁸, A. Drazdauskas⁹, E. Stonkutė⁹, G. Tautvaišienė⁹, J.M. Carrasco^{1,2,3}, E. Masana^{1,2,3},
T. Cantat-Gaudin¹⁰, and S. Blanco-Cuaraesma¹¹

¹ Institut d'Estudis Espacials de Catalunya (IEEC), Gran Capità, 2-4, 08034 Barcelona, Spain
e-mail: juan636@fqa.ub.edu

² Institut de Ciències del Cosmos (ICCUB), Universitat de Barcelona (UB), Martí i Franquès, 1, 08028 Barcelona, Spain

³ Departament de Física Quàntica i Astrofísica (FQA), Universitat de Barcelona (UB), Martí i Franquès, 1, 08028 Barcelona, Spain

⁴ Observatoire de Paris (Meudon) GEPI Batiment 11, Hipparque 5 Place Jules Janssen, 92195, Meudon, France

⁵ INAF - Osservatorio di Astrofisica e Scienza dello Spazio di Bologna, via Gobetti 93/3, 40129, Bologna, Italy

⁶ Instituto de Astrofísica de Canarias, E-38205 La Laguna, Tenerife, Spain

⁷ Universidad de La Laguna, Avda. Astrofísico Fco. Sánchez, E-38205 La Laguna, Tenerife, Spain

⁸ INAF – Osservatorio Astrofisico di Arcetri, Largo E. Fermi 5, 50125 Firenze, Italy

⁹ Institute of Theoretical Physics and Astronomy, Vilnius University, Sauletekio av. 3, 10257 Vilnius, Lithuania

¹⁰ Max-Planck-Institut für Astronomie, Königstuhl 17, 69117 Heidelberg, Germany

¹¹ Harvard-Smithsonian Center for Astrophysics, 60 Garden Street, Cambridge, MA 02138, USA

ABSTRACT

Context. Open clusters provide valuable information on stellar nucleosynthesis and the chemical evolution of the Galactic disc, as their age and distances can be measured more precisely with photometry than for field stars.

Aims. Our aim is to study the chemical distribution of the Galactic disc using open clusters by analysing the existence of gradients with Galactocentric distance, azimuth or height from the plane and dependency with age.

Methods. High-resolution spectra ($R > 60\,000$) of 194 stars belonging to 36 open clusters are used to determine atmospheric parameters and chemical abundances with two independent methods: equivalent widths and spectral synthesis. The sample has been complemented with 63 clusters with high-resolution spectroscopy from literature.

Results. We measure local thermodynamic equilibrium abundances for 21 elements: α (Mg, Si, Ca, and Ti), odd-Z (Na and Al), Fe-peak (Fe, Sc, V, Cr, Mn, Co, Ni, Cu, and Zn), and neutron-capture (Sr, Y, Zr, Ba, Ce, and Nd). We also provide non-local thermodynamic equilibrium abundances for elements when corrections are available. We find inner disc young clusters enhanced in [Mg/Fe] and [Si/Fe] compared to other clusters of their age. For [Ba/Fe] we report an age trend flattening for older clusters (age < 2.5 Ga). The studied elements follow the expected radial gradients as a function of their nucleosynthesis groups, which are significantly steeper for the oldest systems. For the first time, we investigate the existence of an azimuthal gradient, finding some hints of its existence among the old clusters (age > 2 Ga).

Key words. Stars: abundances – Galaxy: open clusters and associations: general – Galaxy: abundances – Galaxy: evolution – Galaxy: disc

1. Introduction

Various processes involved in the formation and evolution of the Galactic disc have left their imprint on the chemo-dynamical properties of the stars that populate it. Several tracers have been used to unveil these processes such as H II regions (e.g., Balsaer et al. 2011; Arellano-Córdova et al. 2020; Méndez-Delgado et al. 2022), planetary nebulae (e.g. Maciel et al. 2007; Stanghellini & Haywood 2018), Cepheids (e.g. Genovali et al. 2014; Luck 2018; Minniti et al. 2020; da Silva et al. 2022), low-mass stars (e.g. Boeche et al. 2014; Anders et al. 2017), massive stars (e.g. Daflon & Cunha 2004; Bragança et al. 2019) or star clusters (e.g., Janes 1979; Friel et al. 2002). Open clusters (OCs) have proved particularly useful as some of their properties such as age and distance can be more precisely determined than for other tracers. Moreover, the OC population covers almost the full disc

lifetime, allowing to trace the overall disc history of star formation and nucleosynthesis (e.g., Friel 2013).

Studies based on OCs have provided valuable information about the chemical distribution of the disc stars, such as a decreasing metallicity with increasing Galactocentric position (e.g., Janes 1979; Bragaglia et al. 2008; Sestito et al. 2008; D’Orazi et al. 2009; Jacobson et al. 2011). However, these initial studies were hampered by the small number of systems studied homogeneously (e.g., Pancino et al. 2010; Jacobson et al. 2011). Other authors built larger samples by compiling values in the literature, but they were limited by their heterogeneity (e.g., Carrera & Pancino 2011; Yong et al. 2012; Donati et al. 2015; Heiter et al. 2015; Netopil et al. 2016). These issues have been overcome in the last years by the *Gaia* mission data (*Gaia* Collaboration et al. 2016) and the massive ground-based spectroscopic surveys to complement them. *Gaia* Collaboration et al.

(2023a) studied a sample of 503 OCs older than 100 Ma within a Galactocentric radius (R_{GC}) of ~ 12 kpc based on the third *Gaia* Data Release (DR3, *Gaia* Collaboration et al. 2023b). Unfortunately, *Gaia* only provides abundances for a few elements due to its medium spectral resolution, $R \sim 11\,500$, and the small wavelength coverage, 845 to 872 nm (*Gaia* Collaboration et al. 2016).

High resolution, $R > 20\,000$, ground-based spectroscopic surveys are providing radial velocities and chemical abundances with a better precision than *Gaia*. Currently, only GES (*Gaia*-ESO survey, Gilmore et al. 2012), APOGEE (Apache Point Observatory Galactic Evolution Experiment, Majewski et al. 2017), and GALAH (GALactic Archaeology with HERMES, De Silva et al. 2015) have published data. GES and GALAH are sampling the Southern Hemisphere, while APOGEE is observing both hemispheres using twin telescopes and instruments. APOGEE and GALAH have not made observations specifically designed to study open clusters, which means that the stars studied are in different evolutionary states and therefore show different abundances due to stellar evolution. In addition, the number of sampled stars varies greatly between OCs, with many of them having abundances for a single star. Of the 150 OCs observed in APOGEE (Myers et al. 2022) only 47 have abundances of at least four stars. In the case of GALAH, from the 75 observed systems (Spina et al. 2021) only 14 OCs have measurements of at least four stars.

GES used two different instruments: GIRAFFE with a spectral resolution similar to APOGEE and GALAH, and UVES (Ultraviolet and Visual Echelle Spectrograph, Dekker et al. 2000) with a spectral resolution of $\sim 47\,000$ covering a wavelength range between 480 and 680 nm. Recently, Magrini et al. (2023, hereafter GES23) have studied a sample of 62 OCs older than 100 Ma acquired with GES-UVES. Their work provides abundances for 25 chemical elements, including a number of neutron capture elements such as Y, Zr Mo or Pr. However, GES has sampled only the Southern Hemisphere, while several key OCs, such as NGC 6791, are only available for Northern observers.

Since 2013, we are systematically observing stars in OCs in the framework of the Open Clusters Chemical Abundances from Spanish Observatories (OCCASO) project. Its main driver is to study the kinematic and chemical evolution of the Galactic disc by measuring radial velocities and detailed elemental abundances. For this purpose, we study at least four red clump (RC) stars by high-resolution spectroscopy, $R > 60\,000$, and covering a large wavelength range, 400 to 900 nm (Casamiquela et al. 2016, hereafter Paper I). Atmospheric parameters and Fe abundances for 115 stars belonging to 18 OCs were determined by Casamiquela et al. (2017, hereafter Paper II). Casamiquela et al. (2019, hereafter Paper III) extended this by deriving abundances of five Fe-peak and five α elements for the same sample. Radial velocities for 336 stars belonging to 51 OCs have been presented by Carrera et al. (2022, hereafter Paper IV).

The present paper is the fifth of the series directly based on OCCASO spectra. We publish chemical abundances for 36 OCs observed until December 2020, doubling the number of OCs published in Paper III. We provide improved abundances for 21 chemical elements and, for the first time in the project, the odd- z elements Na, and Al, the Fe-peak elements Mn, Cu and Zn, and neutron capture elements Sr, Y, Zr, Ba, Ce, Nd.

The paper is organised as follows. The target selection, observations, and data reduction are explained in Sect. 2. The spectroscopic determination of atmospheric parameters is detailed in Sect. 2. The chemical abundance computation methods, solar abundance scale, and cluster abundances are explained in Sect.

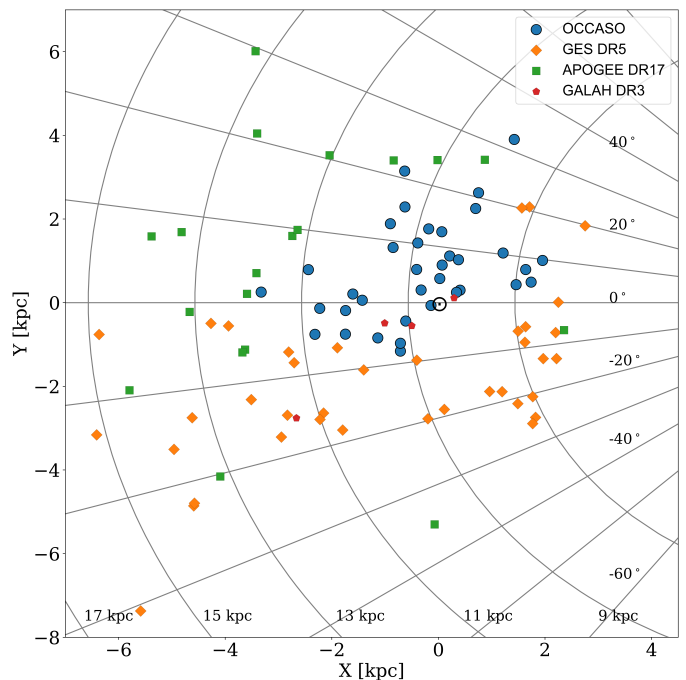


Fig. 1. OCs observed in OCCASO (blue circles) together with OCs complying with similar requirements (at least four observed RC stars and spectral resolution above 20 000) from GES DR5 (orange diamonds), APOGEE DR17 (green squares) and GALAH DR3 (red pentagons). All combined conform the OCCASO+ sample (see Sect. 4).

4. Trends in the Galactic disc are investigated in Sect. 5. Finally, general conclusions are discussed in Sect. 6.

2. Observations and methodology

2.1. Observational material

OCCASO project is dedicated to accurately measuring radial velocities and detailed elemental abundances in OCs, as tracers of the Milky Way disc (see Paper I for details). To reach this goal, it is essential to obtain a sample as large and homogeneous as possible. To this end, OCCASO targets stars at the same evolutionary stage, the RC, to avoid star-to-star abundances variation caused by stellar evolution. RC stars can be easily identified even in sparsely populated colour-magnitude diagrams. They are also brighter than main-sequence stars, allowing us to observe them at further heliocentric distances. Since they are warmer than brighter giants, their spectra are less line crowded, which enables a more accurate determination of atmospheric parameters (effective temperature, surface gravity, and metallicity) and chemical abundances. This requirement constrains our sample to OCs older than 100 Ma, since stars in younger systems have not had enough time to evolve to the RC stage.

In order to obtain representative values from the cluster's average abundances and radial velocities, we target at least four stars per cluster, although in some cases this number can reach up to 12 stars. We adopt this strategy because there is a non-negligible probability of contamination from non-members, even when using membership determined from *Gaia*'s proper motions and parallaxes. Moreover, some targets can be spectroscopic binaries, which complicates their analysis even being real cluster members.

OCCASO employs three high resolution spectroscopic facilities housed at Spanish observatories: the FIBer-fed Echelle

Table 1. Properties of the 36 OCCASO OCs in this work. Positions and ages were computed by Cantat-Gaudin et al. (2020) from *Gaia* DR2 (*Gaia* Collaboration et al. 2018). Examples of abundances derived in the present work and the number of stars studied in each cluster are shown in the last columns of the printed table. The complete table with the LTE abundances of the 21 elements plus the NLTE of those available is published at the CDS.

Cluster	α_{ICRS} [deg]	δ_{ICRS} [deg]	Age [Ga]	Distance [pc]	X [pc]	Y [pc]	Z [pc]	R_{GC} [pc]	[Fe/H] [dex]	[Mg/Fe] [dex]	N
Berkeley 17	80.13	30.574	7.2	3341	-3325	252	-214	11668	-0.24±0.04	0.11±0.28	4
FSR 0278	307.761	51.021	2.2	1708	63	1695	202	8448	0.15±0.05	-0.06±0.03	5
FSR 0850	86.257	24.74	0.5	2232	-2226	-136	-89	10567	-0.01±0.02	-0.03±0.12	3
IC 4756	279.649	5.435	1.3	506	406	299	47	7938	-0.03±0.01	-0.08±0.01	7
NGC 188	11.798	85.244	7.1	1698	-851	1319	646	9285	-0.03±0.07	0.04±0.06	4
NGC 752	29.223	37.794	1.2	483	-324	303	-191	8669	-0.02±0.02	-0.08±0.03	7
NGC 1817	78.139	16.696	1.1	1799	-1742	-189	-405	10084	-0.16±0.03	-0.01±0.02	5
NGC 1907	82.033	35.33	0.6	1618	-1605	207	8	9947	-0.05±0.02	0.00±0.03	4
NGC 2099	88.074	32.545	0.4	1432	-1429	58	77	9769	0.06±0.03	-0.07±0.01	8
NGC 2354	108.503	-25.724	1.4	1370	-713	-1158	-163	9127	-0.03±0.04	-0.03±0.03	6
NGC 2355	109.247	13.772	1.0	1941	-1744	-753	397	10112	-0.10±0.04	-0.02±0.02	6
NGC 2420	114.602	21.575	1.7	2587	-2316	-757	869	10683	-0.22±0.03	0.02±0.02	7
NGC 2539	122.658	-12.834	0.7	1228	-713	-971	236	9105	0.05±0.06	-0.10±0.03	5
NGC 2632	130.054	19.621	0.7	183	-139	-67	98	8479	0.23±0.04	-0.09±0.02	4
NGC 2682	132.846	11.814	4.3	889	-613	-440	470	8964	0.04±0.04	-0.03±0.02	8
NGC 6633	276.845	6.615	0.7	424	339	247	61	8004	-0.02±0.03	-0.06±0.01	4
NGC 6645	278.158	-16.918	0.5	1810	1739	490	-113	6618	0.12±0.03	-0.04±0.05	6
NGC 6705	282.766	-6.272	0.3	2203	1955	1009	-106	6464	0.11±0.07	-0.03±0.03	12
NGC 6728	284.715	-8.953	0.6	1829	1638	791	-181	6747	0.02±0.01	-0.06±0.03	5
NGC 6791	290.221	37.778	6.3	4231	1423	3903	800	7942	0.15±0.14	-0.06±0.25	6
NGC 6811	294.34	46.378	1.1	1161	212	1116	241	8203	-0.03±0.02	-0.06±0.02	6
NGC 6819	295.327	40.19	2.2	2765	754	2628	407	8027	0.04±0.06	-0.05±0.05	4
NGC 6939	307.917	60.653	1.7	1815	-182	1764	386	8703	0.03±0.06	0.00±0.06	5
NGC 6940	308.626	28.278	1.3	1101	376	1026	-137	8029	0.14±0.05	-0.06±0.03	6
NGC 6991	313.621	47.4	1.5	577	26	576	15	8333	-0.03±0.01	-0.06±0.01	3
NGC 6997	314.128	44.64	0.6	901	71	898	-7	8317	0.22±0.07	-0.09±0.01	6
NGC 7142	326.29	65.782	3.1	2406	-628	2288	396	9255	0.00±0.04	-0.06±0.07	4
NGC 7245	333.812	54.336	0.6	3210	-632	3145	-104	9507	-0.01±0.03	-0.09±0.03	5
NGC 7762	357.472	68.035	2.0	897	-408	794	91	8784	0.05±0.07	-0.07±0.02	5
NGC 7789	-0.666	56.726	1.5	2100	-901	1887	-196	9432	0.00±0.07	-0.07±0.02	4
Ruprecht 171	278.012	-16.062	2.8	1522	1458	430	-82	6895	0.14±0.04	-0.05±0.03	6
Skiff J1942+38.6	295.611	38.645	1.5	2378	700	2251	312	7964	0.10±0.06	-0.05±0.06	6
UBC 3	283.799	12.326	0.1	1704	1214	1187	141	7223	-0.01±0.03	0.04±0.02	4
UBC 6	344.01	51.187	0.7	1493	-387	1428	-199	8843	0.02±0.02	-0.08±0.03	6
UBC 59	82.239	48.043	0.5	2585	-2439	789	334	10808	0.03±0.02	-0.02±0.06	3
UBC 215	100.461	-5.243	0.4	1419	-1137	-842	-111	9514	0.08±0.05	-0.10±0.02	5

Spectrograph (FIES) at the Nordic Optical Telescope (NOT) (NOT, Telting et al. 2014, $R \sim 67\,000$, $370 < \lambda < 900$ nm); the High Efficiency and Resolution Mercator Echelle Spectrograph (HERMES) at the Mercator telescope (Raskin et al. 2011, $R \sim 82\,000$, $377 < \lambda < 900$ nm). Both FIES and HERMES are located at the Roque de los Muchachos Observatory in La Palma, Spain. The third instrument is the Calar Alto Fiber-fed Echelle spectrograph (CAFE) installed on the CAHA 2.2m Telescope (Aceituno et al. 2013, $R \sim 62\,000$, $400 < \lambda < 900$ nm), situated at the Centro Astronómico Hispano-Alemán (CAHA) in Almería, Spain.

The data reduction of the observed spectra is fully described in Paper IV. Briefly, bias subtraction, flat-field correction, order tracing, extraction, and wavelength calibration were performed by the dedicated pipelines of each instrument: HERMES DRS for HERMES (Raskin et al. 2011); FIESTool for FIES (Telting et al. 2014); and CAFExtractor for CAFE (Lillo-Box et al. 2020). Our own OCCASO pipeline performs the sky and telluric line subtraction, combination of different exposures, nor-

malisation, and merging of the echelle orders. Additionally, we calculate the radial velocity of the stars by cross-correlation with a template, obtaining measurements with a precision of 10 m s^{-1} . The improvements in the spectra combination procedure, described in Paper IV, have considerably reduced the noise of the final spectra, allowing the detection of weaker lines than in our previous papers.

We use the same sample as described in Paper IV, work in which we discard stars considered as non-members. Additionally, we rejected objects whose spectrum had a signal-to-noise ratio lower than 50 pix^{-1} to ensure a good quality abundance measurement. After this, our sample is formed by 194 stars belonging to 36 OCs, which main features are summarised in Table 1. Figure 1 shows the projection of the studied OCs onto the Galactic plane.

2.2. Methodology

We followed a similar analysis strategy as in Papers II and III. Two different methods are used to compute the atmospheric parameters and chemical abundances: equivalent widths (EW) and spectral synthesis (SS). For the sake of homogeneity, in both cases, we use the MARCS atmosphere models (Gustafsson et al. 2008) and the sixth version of the GES line list (Heiter et al. 2021). We refer the reader to Paper II for details.

For spectral synthesis, we used *iSpec* (Blanco-Cuaresma et al. 2014a; Blanco-Cuaresma 2019), and performed the analysis by comparison between the observed spectrum and synthetic one. The spectra are computed on the fly with the SPECTRUM radiative transfer code (Gray & Corbally 1994). We vary the parameters to be measured until the chi-square value of the fit is minimized. It provides effective temperatures, T_{eff} , surface gravities, $\log g$, microturbulence velocities, v_{mic} , metallicities, $[M/H]$, and rotational velocities, $v \sin i$. We consider that the line broadening is mainly due to rotation, by assuming a negligible macroturbulence velocity, as both broadening mechanisms are difficult to discern in red giants. (e.g., Thygesen et al. 2012). The atmospheric parameters derived with SS are presented in Table A.4.

The equivalent widths are measured by DAOSPEC, a code that detects and fits absorption lines (Stetson & Pancino 2008). We take advantage of the D00p wrapper (Cantat-Gaudin et al. 2014), which allows to batch-process the analysis and to determine the best DAOSPEC input parameters. The resulting EWs are fed to GALA (Mucciarelli et al. 2013), which derives the atmospheric parameters using the WIDTH9 radiative transfer code (Kurucz 2005), using the classical spectroscopic method based on Fe lines. We reject too weak and too strong lines outside the range $-5.9 \geq \log \frac{EW}{\lambda} \geq -4.8$. The atmospheric parameters derived with EW are T_{eff} , $\log g$, v_{mic} , and $[M/H]$ (Table A.4). Unlike the procedure carried out in Papers II and III, we do not perform a normalisation with DAOSPEC, since it is already done during the reduction process. Once the atmospheric parameters have been determined by both methods we compare them and determine the chemical abundances as detailed in Sect. 3.

2.2.1. Line list selection

The sixth version of the GES line list is a compilation of atomic parameters of 80 612 spectral lines (Heiter et al. 2021) covering the whole wavelength range of our spectra. The master line list provides two flags for each line: *gf_flag*, related to the reliability of the transition probabilities of the lines; and *synflag* indicating whether the line is blended or not at the UVES resolution, $R \sim 47\,000$. Both flags can take the values: Y, for “yes, we recommend to use this line”; N, for “not recommended”; or U, for “undecided” (see Heiter et al. 2021, for details). However, we may be able to resolve some lines blended in UVES spectra as OCCASO uses a higher resolution ($R \geq 67\,000$). Therefore, all lines are potentially usable regardless of their *synflag* values, as already suggested by Heiter et al. (2021).

In the case of SS, which is less sensitive to line blends, we determine the atmospheric parameters using lines that lead to consistent abundances in a solar spectrum as described in Paper II. For the determination of atmospheric parameters with EW and abundances in both methods, we select the most suitable lines with the following procedure: First, we discard all lines with *gf_flag*=N since they are considered of low accuracy. Second, we run both methods on the whole sample, selecting lines which are measurable in at least 50 stars. Third, we discard lines yield-

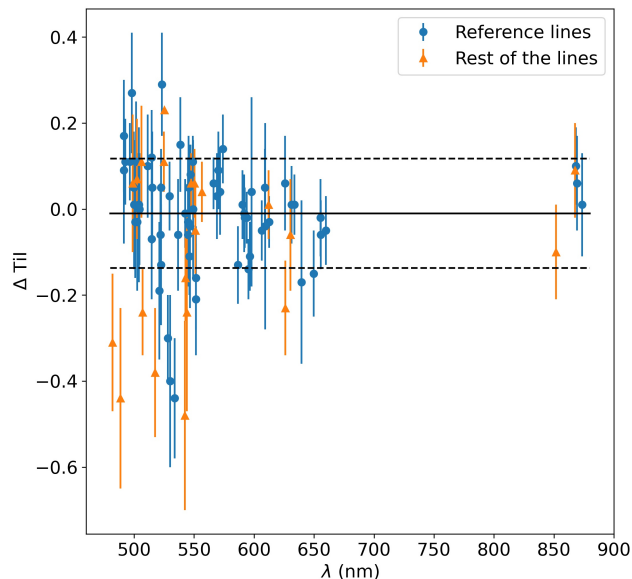


Fig. 2. Difference between the abundance calculated using a given line and the $Ti\ I$ mean abundance represented versus the wavelength of the line. The blue circles are the reference lines, while orange triangles are the others. The distribution of the reference lines is used as selection criteria, keeping those lines that are in the region delimited by $\pm 1\sigma$ (between dotted lines). Ti is used as an illustration; the procedure is the same for all chemical elements.

ing different chemical abundances because of blends or inaccurate atomic parameters. For each element, we calculate the difference between the abundance of each line and the mean abundance. By doing this for all stars, we obtain a distribution for each line, which we evaluate by calculating their median and standard deviation. The lines that have a dispersion higher than 0.25 dex are discarded. In Papers II and III we employ a fixed value to discard lines with discrepant medians. On the contrary, in this work we use reference lines in this process, considering as such those marked as *gf_flag*=Y and *synflag*= Y or U. We evaluate the distribution of their medians and select all the lines in the $\pm 1\sigma$ region (dashed lines in Fig. 2). We repeat the process twice to improve the discarding of lines with discrepant values. The EW and SS line lists are presented in Tables A.1 and A.2, respectively.

For the elements with less than 10 detected lines (Na, Mg, Al, Zn, Sr, Y, Ba, Ce, Zr, and Nd), statistical criteria are not enough to assess the goodness of a line. In this case, we select the best lines by visual inspection of our highest signal-to-noise ratio spectra. Additionally, the Na lines at 589.00 and 589.59 nm, labelled as YY, are discarded because they are contaminated by interstellar medium absorption lines.

2.2.2. Impact of the initial guess values in GALA

GALA requires an initial guess of the atmospheric parameters to start the analysis. In Papers II and III, the same initial guess values were used to analyse the entire sample, $T_{\text{eff}}=4700$ K and $\log g=2.50$ dex. In the present work, we investigate the impact of the initial guess values on the final result. To do that, we initialise the analysis with 21 different combinations of T_{eff} and $\log g$ in a grid covering $4100 \leq T_{\text{eff}} \leq 5300$ K with a step of 200 K,

and $1.4 \leq \log g \leq 3.5$ dex with a step of 0.3 dex. For each combination of initial guess values, we compute the atmospheric parameters of all stars.

We use three independent criteria to evaluate the goodness of the results. First, the merit function provided by GALA, which estimates the quality of the global solution. It is calculated considering the values of the optimisation parameters and the corresponding uncertainties (see Mucciarelli et al. 2013, for details). Second, we evaluate the difference between the derived atmospheric parameters and the initial guess values, selecting the results that satisfy $|T_{\text{eff,guess}} - T_{\text{eff}}| < 100$ K and $|\log g_{\text{guess}} - \log g| < 0.5$ dex. This rules out solutions that converged to values very different from the initial guesses. Finally, we take into account the number of times that a result is obtained for the same star starting from the different guess values. The most repeated result may be the most reliable.

We used the combination of the three criteria to choose the atmospheric parameters for each star. For 151 stars, 78% of cases, the three criteria yield the same atmospheric parameters. These are the most robust EW results, flagged as 1 in column 'GALAF' of Table A.4. For 15% of the cases, two of the criteria pointed to the same atmospheric parameters, while the other provides a different solution. In these cases, we select the solution obtained from two of the criteria. They are flagged as 2 if the results are derived from the first and second criteria and 3, if it is obtained from the second and third criteria. There are no cases with agreement from the first and third criteria. Finally, in the remaining 13 stars, 7% of the sample, every criterion provides a different solution. These cases are flagged as 4, and the adopted result is the one with the best merit function.

2.2.3. Solar abundance scale

To determine the solar abundances, we proceed as in Papers II and III, retrieving the HARPS, UVES and NARVAL solar spectra from the *Gaia* benchmark stars spectral library (Blanco-Cuaresma et al. 2014b). We analyse these spectra with the same methodology as the OCCASO ones and with the two methods, SS and EW. The solar abundances are calculated using the weighted mean of the values derived for each spectrum, with the standard deviation as uncertainty. The abundance values are calculated with the method chosen in Sect. 3.2. The derived values are listed in Table 2. They are consistent, within twice the standard deviation, with the photospheric values obtained by Grevesse et al. (2007) and Asplund et al. (2009). The only exceptions are Na, and Ba with differences of 0.2 and 0.4 dex respectively, being both below 3σ .

3. Results of the spectroscopic analysis

3.1. Atmospheric Parameters

The effective temperatures and surface gravities, derived by each method with their uncertainties, are listed in Table A.4 and compared in Fig. 3. The T_{eff} obtained with SS are slightly higher by 15 ± 80 K than those derived with EW. The typical uncertainties for EW and SS are 55 K and 17 K, respectively. For surface gravity, we find that EW yields values 0.08 dex higher than SS. The standard deviation of the differences is 0.2 dex, which is larger than the average uncertainties for EW, 0.09 dex, and SS, 0.04 dex, respectively. This difference and the dispersion may be explained by the well known difficulties in deriving $\log g$ from spectroscopy, even from high quality and large wavelength coverage spectra as in our case. These results are compatible with

Table 2. Solar abundances calculated in this work, compared with Grevesse et al. (2007, GAS07) and Asplund et al. (2009, AGS09).

Element	This work [dex]	Method	GAS07 [dex]	AGS09 [dex]
Fe I	7.48±0.01	EW	7.45 ±0.05	7.50 ±0.04
Mg I	7.50±0.01	SS	7.53±0.09	7.60 ±0.04
Si I	7.43±0.01	EW	7.51±0.04	7.51 ±0.03
Ca I	6.36±0.01	SS	6.31±0.04	6.34 ±0.04
Ti I	4.91±0.02	EW	4.90±0.06	4.95 ±0.05
Na I	6.49±0.03	SS	6.17±0.04	6.24 ±0.04
Al I	6.55±0.02	SS	6.37±0.06	6.45 ±0.03
Sc II	3.18±0.02	SS	3.17±0.10	3.15 ±0.04
V I	3.90±0.01	SS	4.00±0.02	3.93 ±0.08
Cr I	5.59±0.02	EW	5.64±0.10	5.64 ±0.04
Mn I	5.48±0.02	SS	5.39±0.03	5.43 ±0.05
Co I	4.90±0.02	SS	4.92±0.08	4.99 ±0.07
Ni I	6.27±0.02	EW	6.23±0.04	6.22 ±0.04
Cu I	4.03±0.03	SS	4.21±0.04	4.19 ±0.04
Zn I	4.35±0.02	EW	4.60±0.03	4.56 ±0.05
Sr II	3.03±0.07	SS	2.92±0.05	2.87 ±0.07
Y II	2.08±0.04	SS	2.21±0.02	2.21 ±0.05
Zr II	2.58±0.04	SS	2.58±0.02	2.58 ±0.04
Ba II	2.19±0.02	SS	2.17±0.07	2.18 ±0.09
Ce II	1.45±0.05	SS	1.70±0.10	1.58 ±0.04
Nd II	1.45±0.02	SS	1.45±0.05	1.42 ±0.04

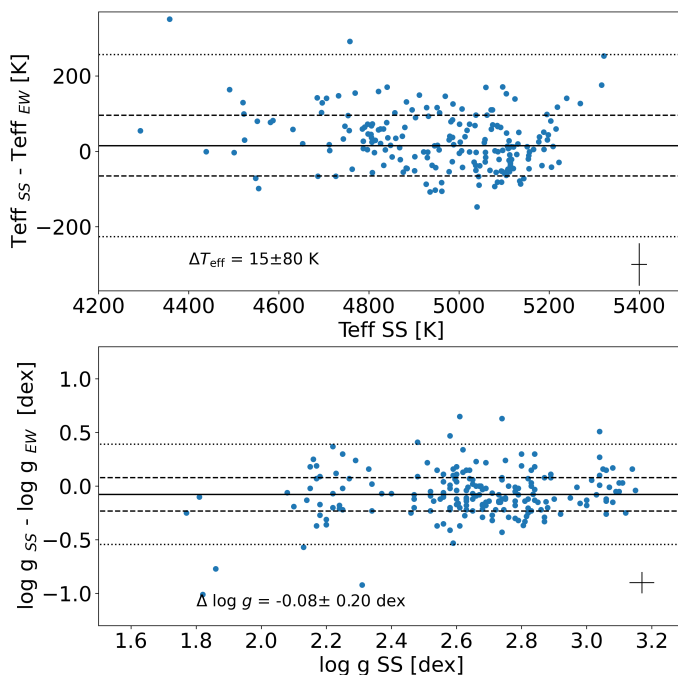


Fig. 3. Differences, in the sense SS-EW, of the T_{eff} (top) and $\log g$ (bottom) as a function of the SS values. Mean difference (solid line), standard deviation (dashed lines), and 3σ levels (dotted lines), are shown in the plot. Typical error bars, calculated as the square of the quadratic sum of each method uncertainties, are shown in the bottom-right corner.

the values obtained in Paper II for a smaller sample. Other studies using different methods find similar differences among methods (e.g., Smiljanic et al. 2014).

Owing to the fact that T_{eff} and $\log g$ values derived from both methods are compatible within the uncertainties, we obtain the weighted average of them, also listed in Table A.4, following the

Table 3. Differences of the atmospheric parameters and abundances for the stars in common with the literature, in the sense ours-others. We only consider those works with more than 10 stars in common. N is the number of stars in common with OCCASO per study and parameter.

Parameter	APOGEE DR17	N	GALAH DR3	N	GES DR5	N	<i>Gaia</i> DR3	N	Jacobson et al. (2011)	N
T_{eff} [K]	26.0±52	49	93.0±51	14	133.0±89	35	127±107	142	79±56	24
$\log g$ [dex]	0.0±0.1	49	0.2±0.1	14	0.0±0.1	35	0.3±0.2	142	0.0±0.1	24
[Fe/H] [dex]	0.0±0.1	49	0.0±0.1	14	0.0±0.1	35	-0.1±0.1	142	0.0±0.1	24
[Mg/Fe] [dex]	0.0±0.1	47	0.0±0.1	14	-0.1±0.1	33			-0.2±0.1	24
[Si/Fe] [dex]	0.1±0.1	49	-0.1±0.1	14	0.0±0.1	35			-0.1±0.1	24
[Ca/Fe] [dex]	0.0±0.1	49	-0.1±0.1	14	0.0±0.1	35			0.1±0.1	24
[Ti/Fe] [dex]	0.1±0.1	49	0.0±0.1	14	0.1±0.2	35			0.2±0.1	24
[Na/Fe] [dex]	0.1±0.1	47	0.0±0.1	14	0.1±0.1	33			0.0±0.1	24
[Al/Fe] [dex]	0.2±0.1	47	0.0±0.1	14	0.0±0.1	33			-0.2±0.1	7
[V/Fe] [dex]	0.1±0.2	47	-0.1±0.1	12	0.0±0.1	33			–	0
[Cr/Fe] [dex]	0.0±0.1	49	0.0±0.1	14	0.0±0.1	35			0.0±0.1	7
[Mn/Fe] [dex]	-0.1±0.1	47	-0.2±0.1	14	0.0±0.1	33			–	0
[Co/Fe] [dex]	0.0±0.1	47	0.1±0.1	14	0.1±0.2	33			–	0
[Ni/Fe] [dex]	0.0±0.1	49	0.0±0.2	13	0.0±0.1	35			0.1±0.1	24
[Cu/Fe] [dex]	–	0	0.0±0.1	14	0.0±0.2	32			–	0
[Zn/Fe] [dex]	–	0	-0.1±0.2	13	0.0±0.1	33			–	0
[Y/Fe] [dex]	–	0	-0.2±0.2	14	0.1±0.1	33			–	0
[Zr/Fe] [dex]	–	0	-0.1±0.1	11	-0.1±0.3	21			-0.1±0.1	7
[Ba/Fe] [dex]	–	0	-0.3±0.2	14	0.1±0.1	31			–	0
[Ce/Fe] [dex]	0.1±0.2	47	–	0	0.1±0.2	32			–	0
[Nd/Fe] [dex]	–	0	-0.2±0.0	12	-0.1±0.1	33			–	0

Notes. Flags of surveys used to select stars for comparison: APOGEE DR17: ASPCAPFLAG = 0 or 4; GES DR5: SFLAGS ≠ SNR,SRP,NIA; GALAH DR3: flag_sp = 0, flag_fe_h=0; *Gaia* DR3 & flags 1-7, 10 and 12 = 0, flag 8 and 9 ≤ 1.

same strategy as in Paper II. Because general metallicity and microturbulence velocity are modelled differently in both methods, we do not attempt to combine them. The average values of T_{eff} and $\log g$ are used to calculate again the microturbulence and overall metallicity in both methods independently, and additionally, the rotational velocity in SS. This procedure decreases the differences between the two methods in the chemical abundance determination (see Paper II). The T_{eff} and $\log g$ uncertainties of each method are added in quadrature to calculate the uncertainties of the average values.

Our sample includes several stars that have also been observed by other spectroscopic surveys. We compared our sample with studies that share a minimum of 10 stars, as shown in Fig. 4 and listed in Table 3: APOGEE DR17 (Abdurro’uf et al. 2022), GALAH DR3 (Buder et al. 2021), GES DR5 (Randich et al. 2022), *Gaia* DR3 GSP-Spec (*Gaia* Collaboration et al. 2023a) and Jacobson et al. (2011). In all cases, star selection was based on different flags provided by each survey, which are described in Table 3.

There is an excellent agreement with APOGEE DR17 within the uncertainties. For GALAH DR3, we obtain slightly larger values, although this comparison is based on only 14 stars. Moreover, the distribution in T_{eff} shows a tail towards negative differences. The difference with T_{eff} from GES DR5 shows a double peaked distribution, which yields a large standard deviation of 89 K. The highest peak shows that our T_{eff} are higher than those provided by GES DR5. In contrast, their $\log g$ values show a good agreement with ours. The comparison with *Gaia* DR3 shows wider distributions, as expected from the larger uncertainties of the *Gaia* measurements, and our values of T_{eff} and $\log g$ are larger. The irregular distribution obtained for the differences in $\log g$ reflects the greater difficulty in deriving gravities from spectroscopy in the small wavelength range covered by *Gaia*.

We performed the comparison after applying the $\log g$ correction proposed by Recio-Blanco et al. (2023). In the case of Jacobson et al. (2011), our T_{eff} are slightly higher than theirs, but $\log g$ values show a good agreement. We have also compared our results with other high-resolution studies ($R \sim 20\,000$) with less than 10 stars in common. There are no clear systematics with any of those studies.

3.2. Stellar chemical abundances

From SS, we determined abundances for 21 chemical elements: Fe, Mg, Si, Ca, Ti, Na, Al, Sc, V, Cr, Mn, Co, Ni, Cu, Zn, Sr, Y, Zr, Ba, Ce, and Nd. Additionally, for those elements with a significant number of unblended lines and not significantly affected by hyperfine or isotopic structure, we also derived abundances from EW for Fe, Cr, Ni, Ti, Si, Ca, and Zn.

The abundances are calculated as the weighted average of the values derived for each individual line. The abundance uncertainties are computed as $\frac{\sigma}{\sqrt{n}}$, being σ the standard deviation and n the number of lines. We take into account the low statistic correction factor in σ by applying the equation 5 of Roesslein et al. (2007). When only one line was measured (Zn, Sr, Zr, and Ce), we adopt the line abundance error as the elemental uncertainty. The abundances computed by both methods are listed in Table A.4.

Several stars in our sample were observed with more than one instrumental configuration. This is used to check the consistency of our results. For Fe abundances, we find mean differences of 0.03 ± 0.04 dex in EW, and 0.02 ± 0.03 dex in SS, in good agreement with the quoted uncertainties. The situation is similar for other elements. Therefore, in the case of stars observed with more than one instrumental configuration, the final abundances are calculated as the weighted mean of the several values ob-

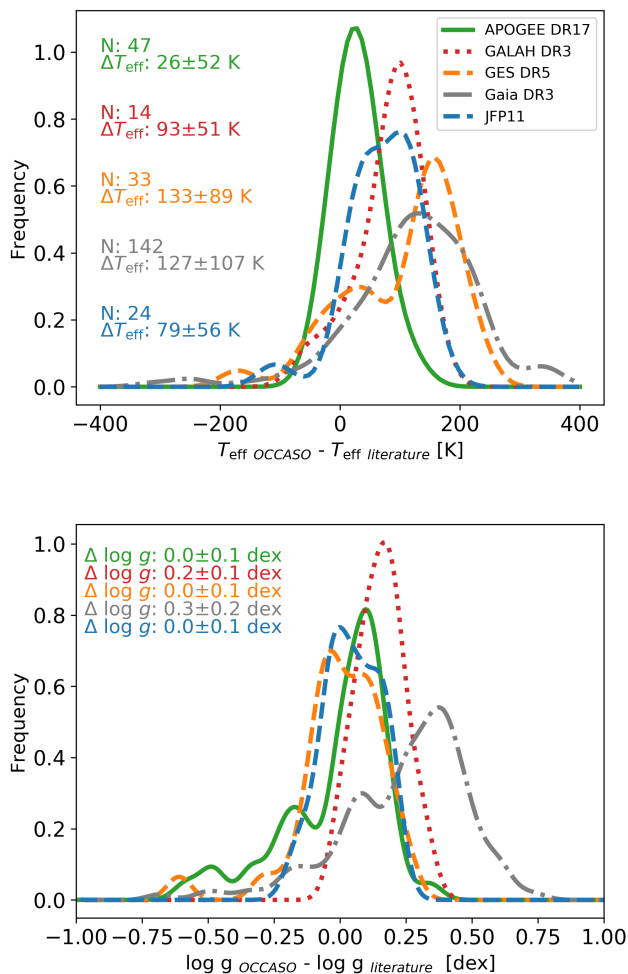


Fig. 4. Distribution of the differences in T_{eff} (top), $\log g$ (bottom) between OCCASO and APOGEE DR17 (green), GALAH DR3 (purple), GES DR5 (orange), *Gaia* DR3 (grey) and Jacobson et al. (2011, JFP, blue). The histogram is smoothed. The mean of the differences and the standard deviation are shown in the panels.

tained. We found correlations with temperature for the elements Si, Na, Al, V, Ni, Sr, Y, Zr, Ba, Ce and Nd having slopes, in absolute value, greater than 1.5×10^{-4} dex/K. This is because in our stars temperature and age are correlated, therefore, as the abundance of these elements depends on age (see sect. 4.2) they will also have a temperature dependence.

Figure 5 shows the distributions of the $[X/H]$ uncertainties of the 21 elements measured in the stars of the sample. The elements from Fe to Ni have mean uncertainties of about 0.05 dex, while from Cu on they have slightly higher uncertainties ~ 0.1 dex. This is explained by the small number of lines measured for these elements. Sr has the most imprecise measurements, with mean uncertainties of 0.15 dex.

In Fig. 6, we compare the derived abundances of the 7 elements studied with the two methods. We find good agreement between methods except in the case of Zn for which, there is a systematic difference of 0.22 ± 0.04 dex. The origin of the difference is unknown. It is not due to the radiative transfer code used in SS since we obtain similar results when we repeat the analysis using Turbospectrum (Plez 2012). The mean difference for Fe abundance is 0.01 dex, with a standard deviation of 0.04 dex. So, we no longer find the difference in Fe abundance found in Pa-

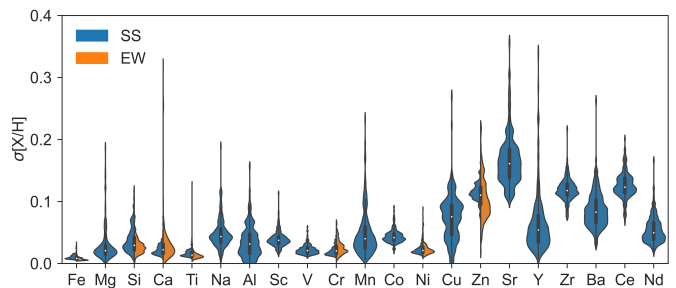


Fig. 5. Distribution of the stellar $[X/H]$ uncertainties of the 21 chemical elements derived with SS or EW methods.

per II of 0.07 ± 0.05 dex. This may be explained by the improvements in the continuum placement implemented in Paper IV, and the improved EW analysis discussed above. The stars that have the largest differences between their abundances measured by the two methods are those with the lowest S/N. When the abundance of an element is measured by both methods, we evaluate the number of used lines, the abundance internal error, and systematic differences with the literature to select which method we rely on the most. We adopt the SS abundances except for Fe, Si, Ti, Cr, Ni and Zn, for which we use the EW determinations.

Table 3 shows the differences with the literature for the studied elements. Only the works with at least 10 stars in common with our sample have been included. For $[\text{Fe}/\text{H}]$, there is an excellent agreement with APOGEE DR17, GES DR5 and GALAH DR3. *Gaia* DR3 shows a systematic difference of -0.1 ± 0.1 dex. We perform this comparison after applying the correction in $[\text{Fe}/\text{H}]$ proposed by Recio-Blanco et al. (2023). We do not find general systematic differences with the literature for the rest of the elements. Furthermore, we have compared our results and other high-resolution studies ($R \gtrsim 20\,000$) that have ten or more stars in common with our sample. Our analysis reveals no evident patterns or consistent discrepancies between these studies and ours.

3.3. Cluster chemical abundances

We adopt the membership analysis performed in Paper IV based on the proper motions and radial velocities. There are 32 stars reported in the literature as spectroscopic binary members (see Paper IV for details). We have checked for the presence of double lines in their spectra using iSpec, but we do not find signs of secondary stars in any of them. We consider their spectra valid for abundance analysis.

The abundance of each cluster is the weighted average of those of its member stars. The associated error is then the standard deviation of the abundances multiplied by the low statistics correction factor (see Sect. 3.2). The full cluster abundances are listed in the full version of Table 1, available at the CDS. In Fig. 7 we show the distribution of standard deviations for each element. For the elements from Fe to Cu, the mean standard deviation is around 0.05 dex, and it is higher for the elements from Zn to Nd. This is a direct consequence of the higher uncertainties measuring those elements. NGC 6791 shows the largest standard deviations because it is the most distant cluster in the sample and has been measured with the lowest S/N.

In Fig. 8 we compare our abundances of Fe and α elements with other high-resolution studies ($R > 20\,000$). In Fig. A.3 we show the comparisons for the rest of the elements. There is a general good agreement with the literature. The differences are at the same level than the ones found in the star-by-star comparison

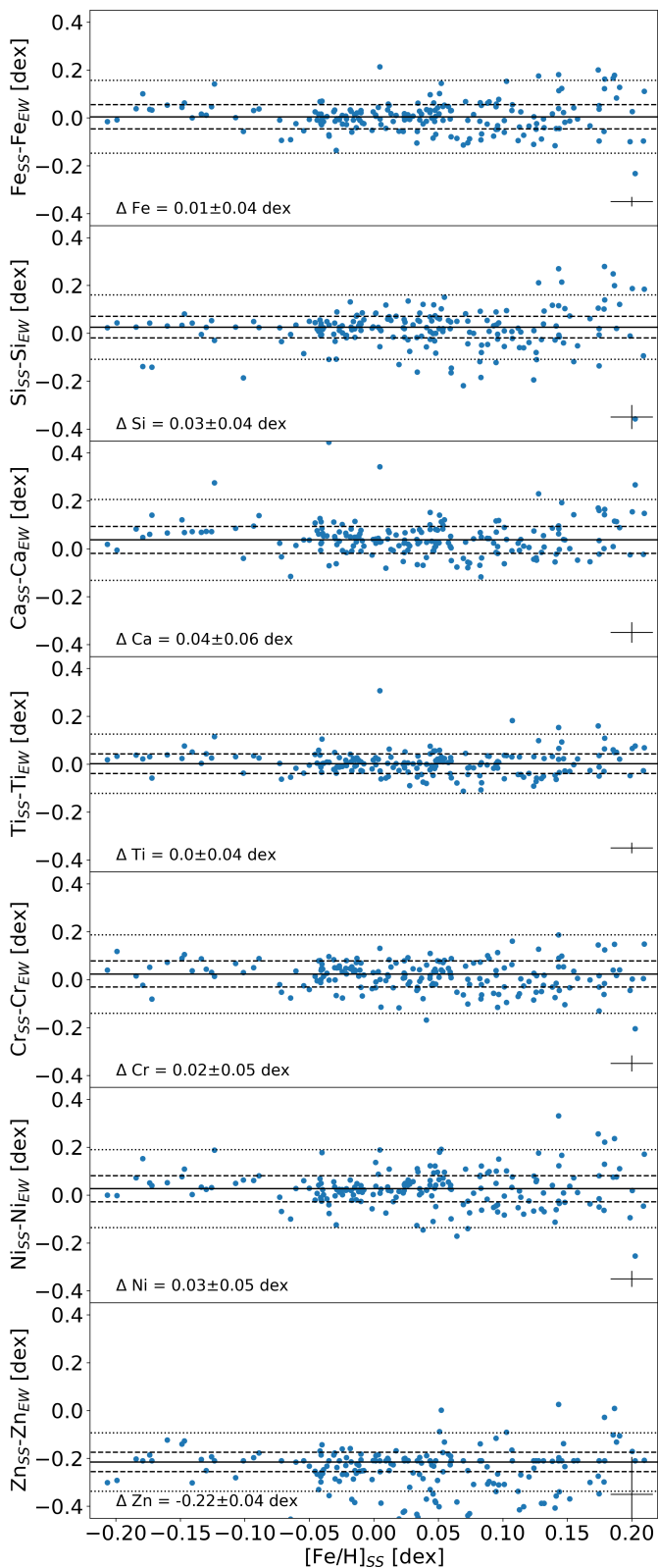


Fig. 6. Differences of the abundances computed by both EW and SS methods versus SS $[\text{Fe}/\text{H}]$ values. The mean differences and standard deviations are shown in each panel. In the bottom-right corner of each panel, we plot the mean uncertainty.

in Table 3. The OC that presents the most considerable difference with the literature is NGC 6791, specially in $[\text{Fe}/\text{H}]$, although the

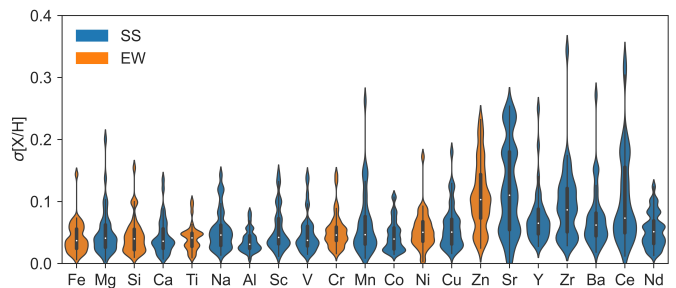


Fig. 7. Distribution of the $[\text{X}/\text{H}]$ standard deviations derived with the SS (blue) and EW (orange) methods for the 36 OCs in our sample.

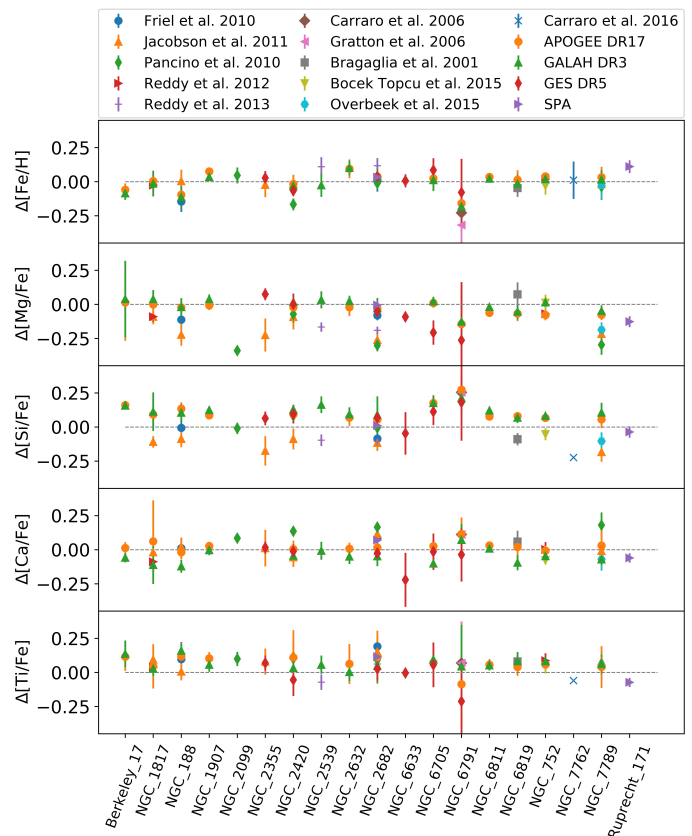


Fig. 8. Comparison of the abundances of Fe and α elements of the OCs in our sample with the literature, in the sense this work minus literature.

values of some studies are compatible with ours considering the errors (e.g., GES DR5). This was already noticed and reported in Paper III.

3.4. Non local thermodynamic equilibrium corrections

Some of the elements could be affected by non local thermodynamic equilibrium (NLTE), so we have reviewed the effect of considering it in our sample. We calculated the corrections for Fe, Mg, Si, Ca, Ti, Cr, Mn and Co using Spectrum Tools¹ that make use of the works of Bergemann et al. (2012), Bergemann et al. (2015), Bergemann et al. (2013), Mashonkina et al. (2007), Bergemann (2011), Bergemann & Cescutti (2010), Bergemann & Gehren (2008) and Bergemann et al. (2010), respectively. We corrected Ba from the results of (Korotin et al. 2015) and Na based on (Lind et al. 2011).

¹ <https://nlte.mpia.de/index.php>

When comparing the results considering local thermodynamic equilibrium (LTE) with NLTE, we find that Fe, Mg (Fig. 9), Si, Ca, Ti, Mn and Ba do not show significant differences when applying NLTE corrections. Cr and Co have slightly higher values when applying NLTE, finding LTE-NLTE differences of -0.06 ± 0.02 dex and -0.03 ± 0.02 dex, respectively. While Na has systematically lower values when correcting for NLTE (Fig. 10) with differences LTE-NLTE of 0.13 ± 0.04 dex. The abundance values per OC applying NLTE are published in the CDS version of Table 1.

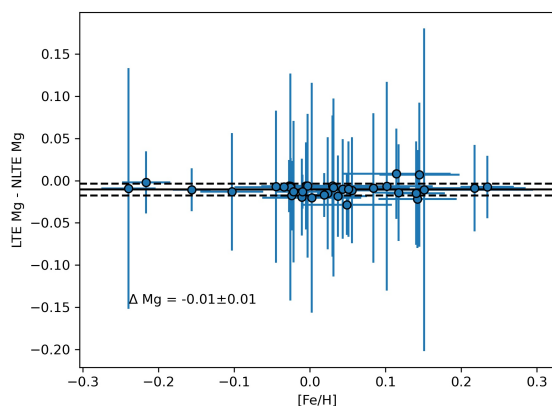


Fig. 9. LTE-NLTE comparison per OC for Mg.

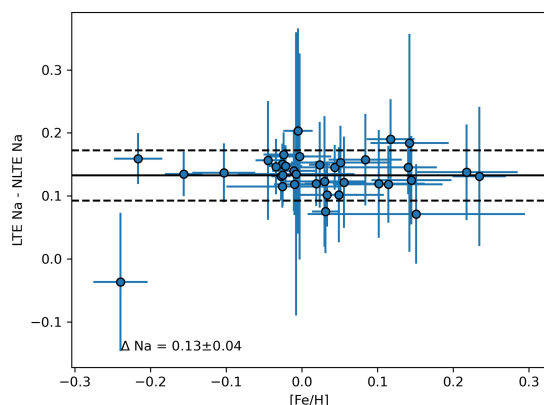


Fig. 10. LTE-NLTE comparison per OC for Na.

4. Galactic trends

We use the mean abundances of our OCs sample in combination with the positions and ages from Cantat-Gaudin et al. (2020), and the orbital parameters derived in Paper IV to investigate the abundance trends in the Galactic disc.

The OCCASO sample provides high-precision abundances derived homogeneously, but it is limited in Galactocentric radius to $R_{GC} < 11.7$ kpc and Galactic azimuth $\phi < -10^\circ$ (Fig. 1). In order to enlarge the spatial coverage, we created OCCASO+ adding OCs from high-resolution ($R > 20\,000$) surveys: GES DR5 (Magrini et al. 2023), APOGEE DR17 (Myers et al. 2022) and GALAH DR3 (Spina et al. 2021). The OCCASO and GES samples complement each other due to their similar spectral res-

olutions and wavelength coverage. Additionally, each one observes a distinct hemisphere, resulting in different Galactic azimuths being studied. APOGEE DR17 covers $0^\circ \leq \phi \leq 30^\circ$ and $R_{GC} > 11$ kpc not covered by OCCASO due to its limiting magnitude.

In all cases, we select OCs that have a minimum of four stars studied in the RC region. For those OCs observed by more than one survey, we prioritised the results with the highest resolution in the following sequence: OCCASO, GES, and APOGEE. Owing to the small number of systems sampled by GALAH, we only select them if they have not been observed by any of the others. As the other works we compare with mostly use LTE values, we use the OCCASO LTE values in this section. We discard the V and Co abundances from Myers et al. (2022) due to their large uncertainties in comparison with OCCASO. In total, OCCASO+ contains 99 OCs: 36 from OCCASO, 40 from GES DR5, 19 from APOGEE DR17, and four from GALAH DR3 (Fig. 1). This means that this sample matches 64% with the GES23 sample, 20% with the high-quality sample from Myers et al. (2022), and 17% with the sample of (Spina et al. 2021). We have analysed the stars of OCs in common between the different surveys and OCCASO by calculating the differences of $[X/Fe]$ values. We do not find any dependence of the abundance differences on atmospheric parameters or $[Fe/H]$. What we find are slight $[X/Fe]$ abundances zero points between studies (Fig. A.3). We apply the abundance offsets to the literature samples so that all abundances are on the same scale. Special attention should be paid to the GALAH abundances, as several of the elements are published with NLTE calculations (Buder et al. 2021). By checking the stars in common (Table 3), we find neither dependencies with atmospheric parameters nor zero points higher than with other surveys. The only exception is $[Ba/Fe]$, for which we find differences around 0.4 dex. NLTE cannot explain these differences (see section 3.4) so the difference between GALAH and OCCASO results must be due to other sources. We have, therefore, used the GALAH abundances in OCCASO+. The way in which OCCASO+ has been selected makes it the most complete sample of OCs with precise abundances. In the following subsections, we analyse different Galactic disc chemical abundance trends with both OCCASO and OCCASO+ samples.

4.1. Abundance dependence on $[Fe/H]$

We plot in Fig. 11 the abundance ratios $[X/Fe]$ versus $[Fe/H]$ for the OCCASO (circles) and OCCASO+ (triangles) samples, colour-coded by age. To make the interpretation easier, the different elements are sorted by their nucleosynthetic group.

All α elements (Mg, Si, Ca, and Ti) show a slightly decreasing trend with metallicity, which is more clear for the OCCASO+ sample since it covers a larger $[Fe/H]$ range. This trend, widely reported in the literature, is explained by the production of α elements mainly in Core Collapse Supernovae (CCS) from massive stars in short timescales in comparison with Fe, which is produced on longer timescales mostly by type Ia Supernovae (SNe Ia). The slopes of each α element can be different because of their different production chains (e.g., Magrini et al. 2017).

The odd- z elements (Na and Al) seem to show a mild decreasing trend at subsolar metallicities up to $[Fe/H] \sim -0.2$. Even though there are large uncertainties involved, the Na abundance seems to increase at super-solar metallicities, while Al trend remains mostly flat. These elements are produced by massive and asymptotic giant branch (AGB) stars, but Na is also synthesised in red giants, and mixing effects bring the Na to the surface. The

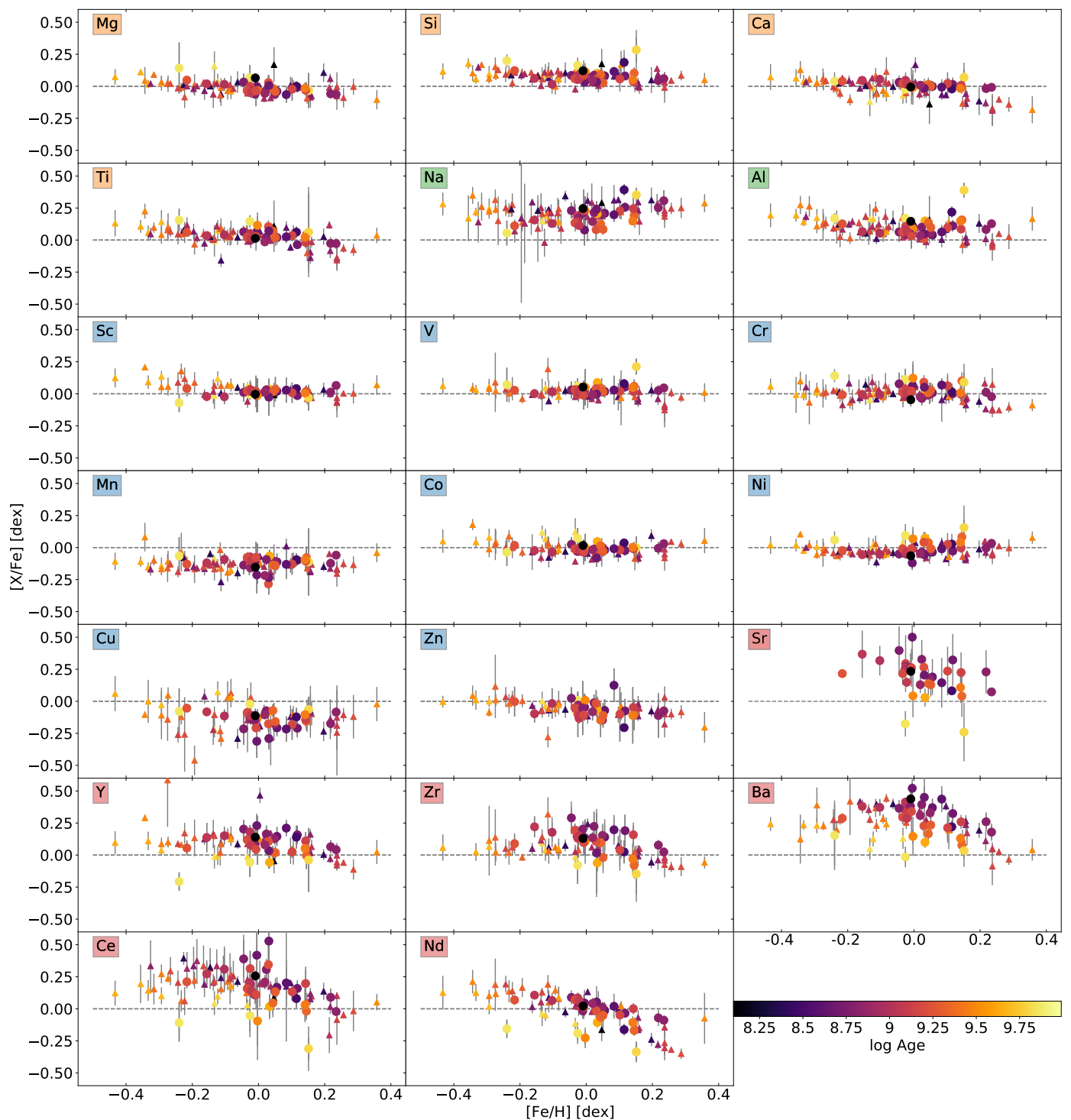


Fig. 11. Abundance $[X/Fe]$ ratios as function of $[Fe/H]$ for OCCASO (circles) and the OCCASO+ (triangles) samples, respectively, colour-coded with the age of the OCs. The colour in the name of the element indicates the nucleosynthetic group: α (orange), odd-Z (green), Fe-peak (blue) and neutron-capture (pink).

process is more important in massive giants, and thus Na can appear enhanced in young OCs (see Sect. 4.2).

The Fe-peak elements (Sc, V, Cr, Mn, Co, Ni, Cu, Zn) are likely to be produced by different nucleosynthesis processes. On the one hand, Sc, V, Cr, Mn, Co and Ni are thought to be produced by the same processes as Fe (Kobayashi et al. 2020), with a trend generally flat. Nevertheless, Sc and Co show mild decreasing trends at low metallicities, similarly to Al. On the other

hand, the nucleosynthesis of the elements Cu and Zn is under debate (Bisterzo et al. 2005; Romano & Matteucci 2007; Prantzos et al. 2018; Kobayashi et al. 2020). The different processes suggested relate their formation to massive stars. Cu exhibits a larger scatter, which may be attributed to higher uncertainties (computed as the abundance standard deviation), making it difficult to extract further conclusions. However, Zn appears to show

a decreasing trend with Fe abundance, that could be compatible with its formation in massive stars.

Neutron capture elements (Sr, Y, Zr, Ba, Ce, and Nd) show larger scatters than the others, mostly due to their age dependence (see Sect. 4.2), and also because of their larger uncertainty. These elements can be produced by slow (s) or fast (r) processes of neutron capture. They are defined by whether the capture timescale is longer or shorter than β decay, and occur at different astrophysical sites. The s-process occurs mainly in AGB stars (e.g., Gallino et al. 1998), while the origin of the r-process is still under debate (e.g., Kajino et al. 2019). All neutron-capture elements studied in this work are produced by both processes, with different relative contributions. They all show similar general behaviour with a dependence on age, being older OCs more depleted. Y, Zr, Ba, and Ce show a slight increasing trend with [Fe/H], reaching their maximum at [Fe/H] \sim 0 dex to decrease again more abruptly at higher [Fe/H] abundances. This last decrease is explained since as [Fe/H] increases, the ratio of neutrons to Fe in AGB star decreases. As a result, there is a smaller proportion of s-process elements being produced (Gallino et al. 2006; Cristallo et al. 2009; Karakas & Lattanzio 2014). Nd is the element which has the highest percentage production by r-process, 38% according to Prantzos et al. (2020). It shows a steeper and more continuous decreasing trend with [Fe/H] compared to the other elements, which can be a consequence of its higher production by r-process.

The obtained abundances patterns are generally compatible with those previously reported in the literature for thin disc stars (e.g., Adibekyan et al. 2012; Delgado Mena et al. 2017, 2019; Mikolaitis et al. 2019; Tautvaišienė et al. 2021). However, the increase of [Mn/Fe] with [Fe/H] reported in the literature (e.g., Adibekyan et al. 2012; Mikolaitis et al. 2019) is not clearly seen in our case. We also find differences in the neutron capture maximum abundance compared to what is stated in the literature. While Delgado Mena et al. (2017) finds it at [Fe/H] \sim 0 dex for the five elements similarly to us, Tautvaišienė et al. (2021) finds the maximum around -0.2 dex for Ba and Ce. In general, for one-zone Galactic chemical evolution models, the maximum is predicted at lower Fe abundances than seen in the observations (e.g., Bisterzo et al. 2017; Prantzos et al. 2018; Kobayashi et al. 2020).

4.2. Abundance dependence on age

We plot the dependence of the different elements with age in Fig. 12 where OCs are colour-coded by their [Fe/H] abundance. For each element, we perform a linear fit to quantify its age dependence. These fits were performed by the same method as in Anders et al. (2017), using a maximum likelihood algorithm as first guess, and computing a Markov-Chain Monte-Carlo with the python package *emcee* (Foreman-Mackey et al. 2013). The results of all fits are listed in the Table A.3. The best fits for both OCCASO and OCCASO+ samples are overplotted in Fig. 12, with green and black lines, respectively.

From Mg to Co, we see very small dispersions, highlighting the small variability of these abundance ratios in the age and metallicity range covered by OCs of the thin disc. Nevertheless, due to the high-precision of our abundances (which is maximised thanks to the number of stars per cluster) we are able to see some mild trends.

In particular, we obtain positive slopes for the α elements Si and Mg, which has been reported in the literature using high-precision samples of field stars (e.g., Delgado Mena et al. 2019). Furthermore, we have noticed enhanced levels of these elements

in several young inner disc OCs aged between 0.1 to 0.7 Ga. Specifically, increased levels of Mg are observed in NGC 6067, NGC 6259, and UBC 3 OCs, while higher Si levels are found in NGC 6067 and NGC 6705 OCs. In the literature, the cluster NGC 6705 was found to be α enhanced (Magrini et al. 2014; Casamiquela et al. 2018), and was considered as a peculiar OC. To our knowledge, this is the first time that NGC 6705 is reported to belong to a group of α enhanced clusters in the inner disc.

The two odd-Z elements Na and Al have different behaviours. Al shows an overall increasing trend consistent with the results of Delgado Mena et al. (2019). Na is mostly flat, though we remark a mild enhancement at young ages until \sim 1.8 Ga, and a plateau for older ages. The Na-enhancement can be explained by the fact that the atmospheres of massive red giant stars (1.5-2 M_{\odot}) are polluted after the first dredge-up because of deep mixing (Smiljanic et al. 2016; Lagarde et al. 2012). As a consequence, OCs younger than \sim 1.2–2.5 Ga can appear enhanced in Na (see also Casamiquela et al. 2020).

Fe-peak elements show some variability in their trends as a function of age, with part of them being positive in both fits, in particular V, Co, Ni, Cu and Zn. Mikolaitis et al. (2019) have also found clear positive trends for Co and Ni in agreement with us, but they find a negative trend for Cu and Mn, in contrast with our results. On the other hand, Delgado Mena et al. (2019) reports similar trends as ours in Cu and Zn.

Neutron capture elements are known to have high dependencies with age. We find steep decreasing trends for all the elements comparable to what has been found in the literature, in particular, Casamiquela et al. (2021) which used a sample of 47 OCs that included most of the OCCASO sample. The trends are also in agreement with those found by Viscasillas Vázquez et al. (2022) for GES OCs, and those reported by Spina et al. (2016) and Delgado Mena et al. (2019) for field stars. The enhancement of s-process elements in young stars is tentatively explained in chemical evolution models by assuming enhanced AGB yields of low-mass stars (e.g., D’Orazi et al. 2009; Cristallo et al. 2015). These low-mass stars may take several Ga to deliver their chemical products into the interstellar medium, leading to a delay in the enrichment of s-process elements, and therefore, to a strong [X/Fe]-age dependence. What is more, the age dependence does not have to be monotonic. In the trend of Ba and possibly Zr there is a hint of a flattening at ages older than \sim 2.5 Ga (see Fig. 12). A similar flattening is reported for Ce by Sales-Silva et al. (2022) from the APOGEE DR17 OC sample, but at 4 Ga. This kind of non-monotonic trend could be caused by a change in the enrichment rate of the interstellar medium by AGB stars. However, we also recall that the computation of Ba abundances can significantly be affected by activity in young stars (Reddy & Lambert 2017; Spina et al. 2020), which can alter the Ba trend with age.

Each element has a different trend according to the ratio at which it is formed by s- and r- processes, as shown in Fig. 13. The slopes get steeper with increasing contribution of s-process. This dependence has also been found for solar twins (Spina et al. 2016) and field stars (Delgado Mena et al. 2019). It can be explained by the different production timescales of the two processes. Unlike the s-process, r-process is expected to occur on short timescales, shorter than those of Fe production. Therefore, the more an element is produced per s-process, the steeper its [X/Fe]-age dependence would be. Several authors calculate the s-process contribution (e.g., Bisterzo et al. 2014; Prantzos et al. 2020), giving different values. The element for which their results differ the most is Sr, being 68.9% at Bisterzo et al. (2014) and

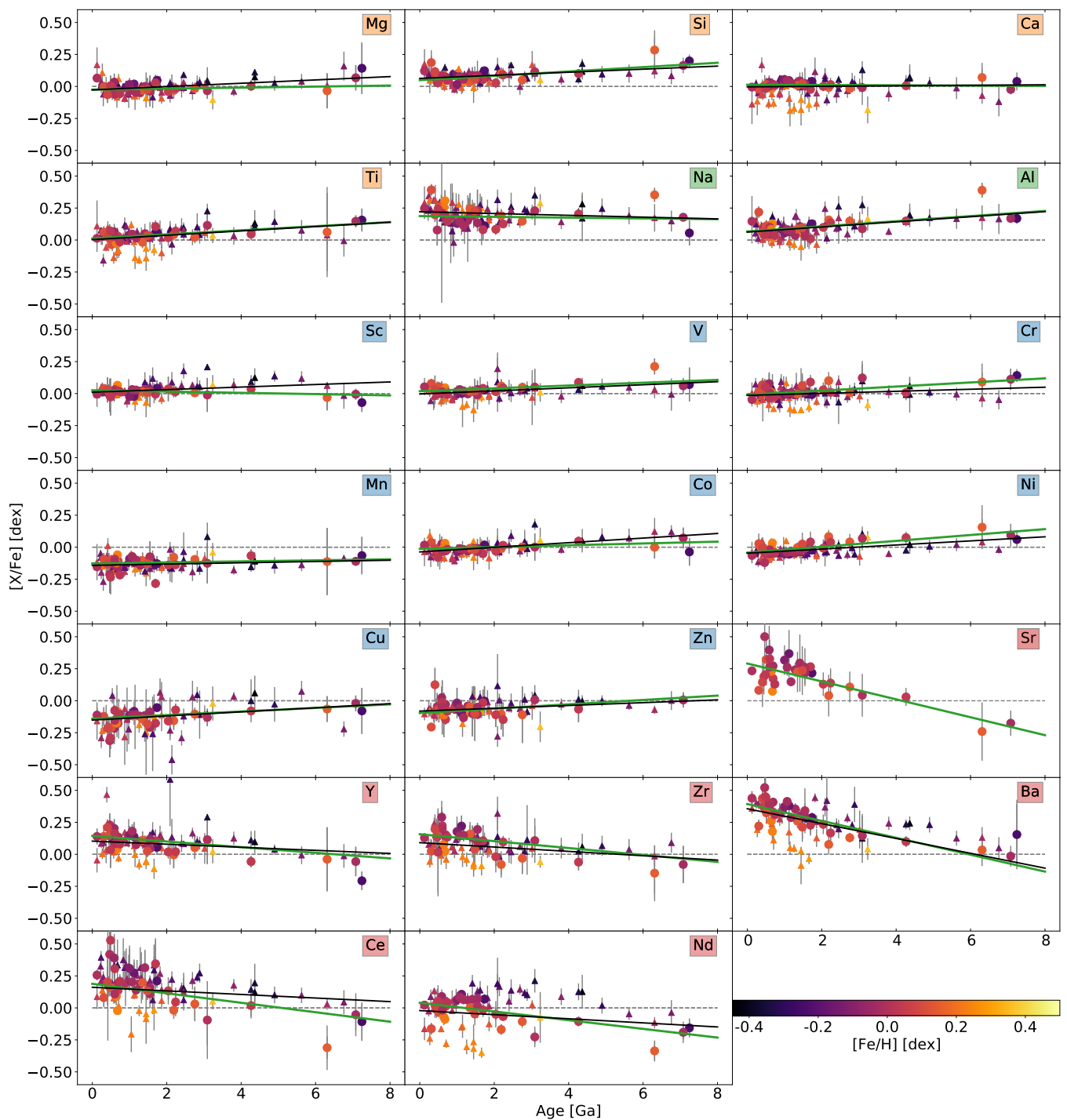


Fig. 12. $[X/Fe]$ ratios vs age, colour-coded as a function of $[Fe/H]$. The symbols and panels are equivalent to Fig. 11. The best fits for OCCASO (green) and OCCASO+ (black), respectively, are plotted.

91.2% at Prantzos et al. (2020). Our results agree better with the value of Prantzos et al. (2020).

4.3. Radial trends

In this section, we study the dependencies on the R_{GC} of $[Fe/H]$ and abundance ratio to Fe of the rest of the elements. The radial distribution of $[Fe/H]$ is one of the most widely used tracers in Galactic archaeological studies. The general consensus is that there is a steeper decreasing gradient in the inner disc and a plateau in the outer regions, the so-called knee shape. In this sec-

tion, we investigate the radial trends on $[Fe/H]$ vs R_{GC} obtained with the OCCASO and OCCASO+ sample. We use the fitting procedure described in Sect. 4.2, but in the case of OCCASO+ we model the fit with two lines, adjusting at the same time the knee position. The OCCASO sample contains only OCs inside the knee. Table 4 contains the slopes obtained with both samples compared to recent literature studies. The knee position derived with OCCASO+ is 11.3 ± 0.8 kpc which confirms the position found in the latest studies in the literature. The results obtained for both OCCASO and OCCASO+ samples inside the knee are compatible with previous determinations in the literature. Out-

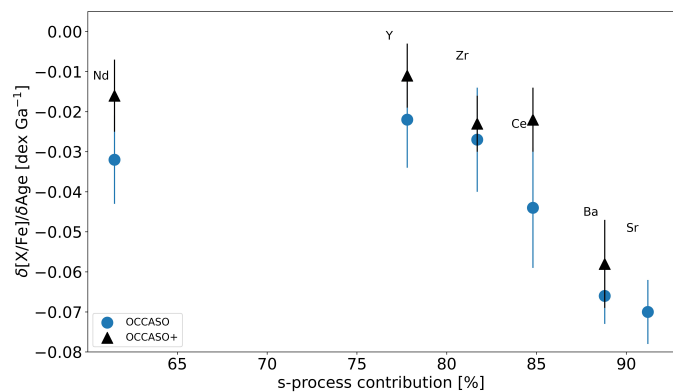


Fig. 13. Slopes of the $[X/Fe]$ -age relations of the neutron-capture elements as a function of their s-process contribution percentages computed by Prantzos et al. (2020).

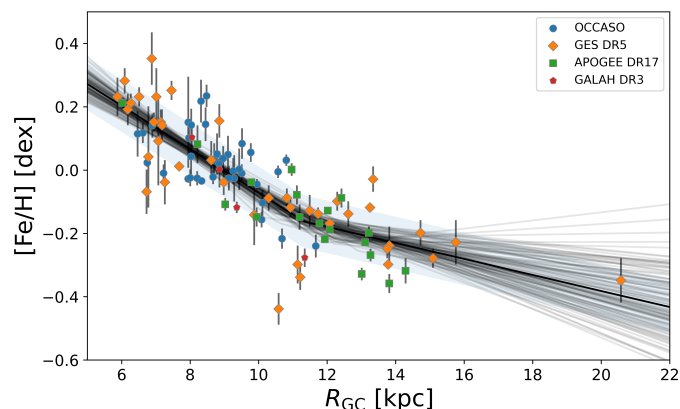


Fig. 14. $[Fe/H]$ versus Galactocentric radius for OCCASO+ sample. The different surveys are colour-coded as in Fig. 1. The grey vertical lines represent the uncertainties of abundances, and the black line represents our best fit.

side the knee, we recover a flatter trend for OCCASO+ in comparison with GES23, and more similar to Spina et al. (2022), Myers et al. (2022) and Carrera et al. (2019). We remark that this result is independent of the inclusion of Berkeley 29, the furthest cluster in the sample.

In Fig. 15 we show the dependence of the different studied elements $[X/Fe]$ with R_{GC} for the OCCASO (circles) and OCCASO+ (triangles) samples and their corresponding linear fits (green and black). The OCCASO+ sample has been fitted with two lines as in the case of the $[Fe/H]$ trends. We have limited the sample to 16 kpc, since at larger distances we only have one cluster in the sample, and therefore this region is not sampled correctly. The code used allows us to determine if a knee shape is found or not. For more than half of the elements, there is no knee shape, and we fit the whole sample with a single line. We find a knee shape for the elements Ti, Na, Cr, Y, Zr, Ba, Ce, and Nd. The results of the analysis are listed in Table A.6.

The α elements show mild positive gradients, more evident for Ca Mg, and Ti. This is in agreement with the models of the inside-out formation of the Galactic disc. The differences among the elements, as already mentioned, are due to their different detailed production processes.

The odd- z elements show different behaviours. Al has a flat relation whereas Na shows a decrease up to 10 kpc showing a positive trend from there off. As already discussed, the en-

richment of the Na atmospheric abundances along the red giant phase makes difficult to reach further conclusions.

Analogous to the discussion in Sect. 4.1, we expect Fe-peak elements produced by the same processes as Fe to have flat radial gradients. We observe this for V, Mn, Co, and Ni inside the knee. However, Cr shows a positive gradient inside the knee, which seems to decrease again outside it. On the contrary, we note that Sc shows a flat trend in the OCCASO sample and a positive trend in the OCCASO+ sample. Additionally, elements mainly produced in massive stars should exhibit positive radial trends, as some α elements do. It could also be the case for Zn, showing a positive trend in the whole studied range.

In the case of the neutron-capture elements, we see again larger dispersions at a given R_{GC} due to their age dependence and larger uncertainties. They tend to show positive gradients, possibly due to the dependence of s-process production with metallicity. However, there are significant differences among them in agreement with the fact that each element is produced in different proportions by r- and s-processes as discussed on Sect. 4.2. We find flatter trends for Sr, Y, Zr, and Ce, and steeper trends for Ba and Nd. In general, the trends are flatter outside the knee for all the elements. That is due to the dependence of s-process on $[Fe/H]$ previously discussed. In the case of Sr we do not know if it happens, as we have no observations outside the knee.

In order to compare our results with the latest studies, we have analysed the samples published by GES23, Myers et al. (2022), Spina et al. (2021) and OCCASO+ restricting the analysis to the same R_{GC} range that in OCCASO sample. The comparison is shown in Fig. 16. Overall, we find good agreement between the different samples taking into account the uncertainties, although there are a few exceptions. We highlight that we find large differences between Spina et al. (2021) and our sample in Ca and Na, and between Myers et al. (2022) and our sample in Na, Co, and Ce. The different slope of Co may be due to the dispersion and high uncertainties of the APOGEE abundances in this element. We also find remarkable differences of Ca, Al, Cu, V, and Zn gradients for GES23 compared with the other samples. For some of these elements (Ca, Ti, Al, and V) the difference in the gradient is due to the fact that in the inner disc ($R_{GC} \leq 8$ kpc) some OCs in GES23 tend to have lower abundances compared to other surveys (see Fig. A.2). Some of these OCs in GES23 are in common with Myers et al. (2022) (Trumpler 20 and Ruprecht 134), which does not confirm their low abundances. Indeed, GES23 abundances of those OCs are ~ 0.07 dex lower than Myers et al. (2022) values. Given the way in which the OCCASO+ sample is constructed, we believe that its results are the most robust and reliable.

4.4. The temporal evolution of Galactocentric radial gradients

In order to investigate the change of the $[Fe/H]$ radial gradient with time, we consider OCs with $R_{GC} < 16$ kpc for the reasons given above, and we divide the samples used in Sect. 4.3 into four age bins: 0.1-1, 1-2, 2-3, >3 Ga, respectively. We maintain the same analysis methodology, providing the slopes of the two fitted lines and the knee position for each age bin (listed in Table 5). The OCCASO+ sample shows the absence of knee in the youngest bin, and its presence in older clusters (see Fig. A.1). By studying the slope inside the knee, the OCCASO+ sample shows a steepening of the trend with age that seems to be non-linear (Fig. 17), since the second age bin has a steeper gradient than expected considering the other age bins. We have tested that this non-linear dependence still appears when we change the way we partition the clusters into age bins. The slope outside the knee

Table 4. Comparison of [Fe/H] radial gradient with the literature in the region inside and outside the knee radius and globally, indicating in each case the number of OCs studied and the knee position.

Reference	Inside the knee radius [dex kpc ⁻¹]	<i>N</i>	Outside the knee radius [dex kpc ⁻¹]	<i>N</i>	Global [dex kpc ⁻¹]	<i>N</i>	Knee [kpc]
This work OCCASO	-0.059±0.017	36	–	–	–	–	–
This work OCCASO+	-0.069±0.008	71	-0.025±0.011	28	-0.062±0.007	99	11.3 ± 0.8
Paper III	-0.056±0.011	18	–	–	–	–	–
Carrera et al. (2019)	-0.077±0.007	–	-0.018±0.009	–	-0.077±0.007	90	11
Donor et al. (2020)	-0.068±0.004	68	-0.009±0.011	3	–	71	13.9
Zhang et al. (2021)	-0.066±0.005	157	-0.032±0.007	4	–	161	14
Myers et al. (2022)	-0.073±0.002	51	-0.032±0.002	34	-0.055±0.001	85	11.5
GES23	-0.081±0.008	42	-0.044±0.014	20	-0.054±0.004	62	11.2
Spina et al. (2022)	-0.064±0.007	–	-0.019±0.008	–	–	–	12.1 ± 1.1
Netopil et al. (2022)	-0.063±0.004	116	–	–	-0.058±0.005	136	12
Gaia Collaboration et al. (2023a)	-0.054±0.008	503	–	–	–	–	–

Table 5. Change with age of the [Fe/H] radial gradients studied through MCMC at Sect. 4.3. The columns b1 and m1 are the y-intercept and slope of the first line fitted, respectively. The column m2 is the slope of the second line. The position of the knee, the number of OCs and Spearman correlation coefficient are listed in the last columns. We analyse the OCCASO and OCCASO+ samples and reanalyse the others. The OCCASO and *Gaia* DR3 samples do not have clusters beyond the knee, so only the first line is fitted. In the first bin of all the samples, we did not find the knee shape.

Sample	Age bin [Ga]	b1 [dex]	m1 [dex kpc ⁻¹]	m2 [dex kpc ⁻¹]	Knee [kpc]	<i>N</i>	Spearman
OCCASO	0.1-1	0.365 ± 0.211	-0.032 ± 0.022			15	-0.30
OCCASO	1-2	0.457 ± 0.084	-0.079 ± 0.015			11	-0.44
OCCASO	2-3	0.347 ± 0.285	-0.054 ± 0.037			4	-0.47
OCCASO	3-7.3	0.828 ± 0.553	-0.099 ± 0.023			5	-0.95
OCCASO+	0.1-1	0.452 ± 0.062	-0.049 ± 0.006			39	-0.75
OCCASO+	1-2	0.795 ± 0.114	-0.09 ± 0.014	-0.019 ± 0.018	10.1 ± 0.8	29	-0.87
OCCASO+	2-3	0.651 ± 0.275	-0.075 ± 0.033	-0.042 ± 0.017	9.6 ± 2.1	14	-0.85
OCCASO+	3-8	0.996 ± 0.305	-0.113 ± 0.034	-0.012 ± 0.018	10.9 ± 1.1	15	-0.80
Myers et al. (2022)	0.1-1	0.395 ± 0.087	-0.051 ± 0.008			39	-0.72
Myers et al. (2022)	1-2	0.673 ± 0.135	-0.08 ± 0.016	-0.041 ± 0.01	10.1 ± 1.0	20	-0.90
Myers et al. (2022)	2-3	0.687 ± 0.177	-0.085 ± 0.017	-0.014 ± 0.026	11.9 ± 0.9	11	-0.77
Myers et al. (2022)	3-8	1.455 ± 0.329	-0.161 ± 0.035	-0.025 ± 0.017	10.8 ± 0.6	12	-0.70
Spina et al. (2021)	0.1-1	0.558 ± 0.062	-0.065 ± 0.006			57	-0.72
Spina et al. (2021)	1-2	0.566 ± 0.187	-0.068 ± 0.019	-0.037 ± 0.047	11.5 ± 1.3	22	-0.86
Spina et al. (2021)	2-3	0.83 ± 0.234	-0.097 ± 0.024	-0.019 ± 0.028	11.9 ± 1.1	10	-0.93
Spina et al. (2021)	3-7.3	1.307 ± 0.295	-0.147 ± 0.032	-0.02 ± 0.018	11.1 ± 0.8	16	-0.82
GES23	0.1-1	0.356 ± 0.057	-0.043 ± 0.006			23	-0.82
GES23	1-2	0.811 ± 0.152	-0.09 ± 0.019	-0.02 ± 0.026	10.8 ± 1.0	17	-0.85
GES23	3-7.3	1.025 ± 0.34	-0.118 ± 0.038	-0.014 ± 0.017	10.7 ± 1.1	12	-0.75
<i>Gaia</i> DR3	0.1-1	0.384 ± 0.069	-0.043 ± 0.005			303	-0.43
<i>Gaia</i> DR3	1-2	0.588 ± 0.196	-0.065 ± 0.01			48	-0.55
<i>Gaia</i> DR3	2-3	0.933 ± 0.392	-0.079 ± 0.025			25	-0.41
<i>Gaia</i> DR3	3-7.3	0.354 ± 0.26	-0.105 ± 0.021			13	-0.54

remains constant, taking into account errors. By re-analysing the other samples, we obtain values compatible with OCCASO+, which is a confirmation of the dependence we find. This is an effect that does not appear in field stars, as has been found in the studies such as Casagrande et al. (2011); Anders et al. (2017, 2023). They show a steepening of the gradient between 1 and 2 Ga to become progressively flatter at older ages, contrary to OCs. The flattening of the gradient is an expected effect of radial migration.

There are two hypotheses that attempt to explain the change in the gradient with age in OCs: Anders et al. (2017) proposed that the change of trend is produced by the radial migration pro-

cess coupled with a selective bias that the Galaxy exerts on OCs. Only outward migrating clusters survive because the Galactic potential becomes less destructive as the distance from the centre increases. Inward migrating clusters are quickly disrupted. Otherwise, GES23 show in their Fig. 5 that young clusters (<1Ga) in the inner disc have lower Fe abundances than older OCs, and propose that a considerable infall of gas with low metallicity has produced the last episode of star formation. In the OCCASO sample, we do not clearly see this age separation. In fact, there are two young OCs in the inner disc that are metal-rich: NGC 2632 and NGC 6997 in contradiction with this hypothesis

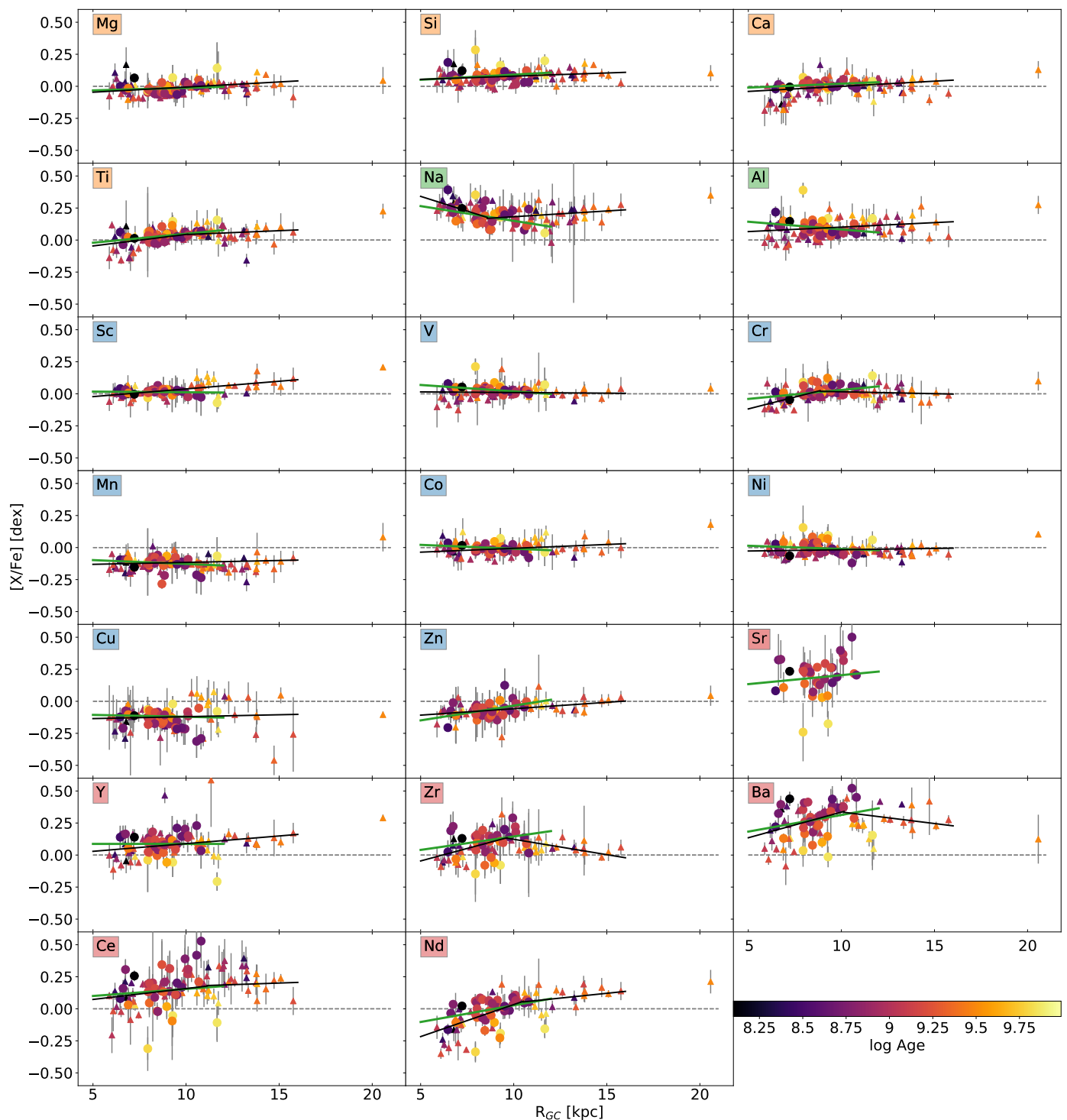


Fig. 15. Abundance $[X/Fe]$ ratios as function of R_{GC} for the OCCASO (circles) and OCCASO+ (triangles) samples colour-coded with age of the OCs. Fitted lines for both samples are shown in green and black, respectively.

(Fig. A.1). This should be studied further, with larger samples in the inner disc.

Another issue for which there is still no satisfactory explanation is the presence of the plateau in the radial gradient. This feature is seen in OCs, and recently in cepheids (da Silva et al. 2023). Similar hypotheses to the ones above have been suggested to explain it: Magrini et al. (2009) suggested that merger events or infall from the halo, affecting large radii and providing pre-enriched material, could explain the plateau. Another possible

explanation is that the plateau is produced by radial migration of OCs towards the outer disc. We do not know the event or mechanism that could have produced it, though. The OCCASO+ sample shows no plateau in the youngest age bin (<1 Ga), with OCs extended up to 14 kpc. We have ruled out that we have a radial bias in the sample, as in the Cantat-Gaudin et al. (2020) catalogue this is the maximum distance at which clusters appear in this age range. As the knee formation event does not affect young clusters, it must be a process that occurred more than 1

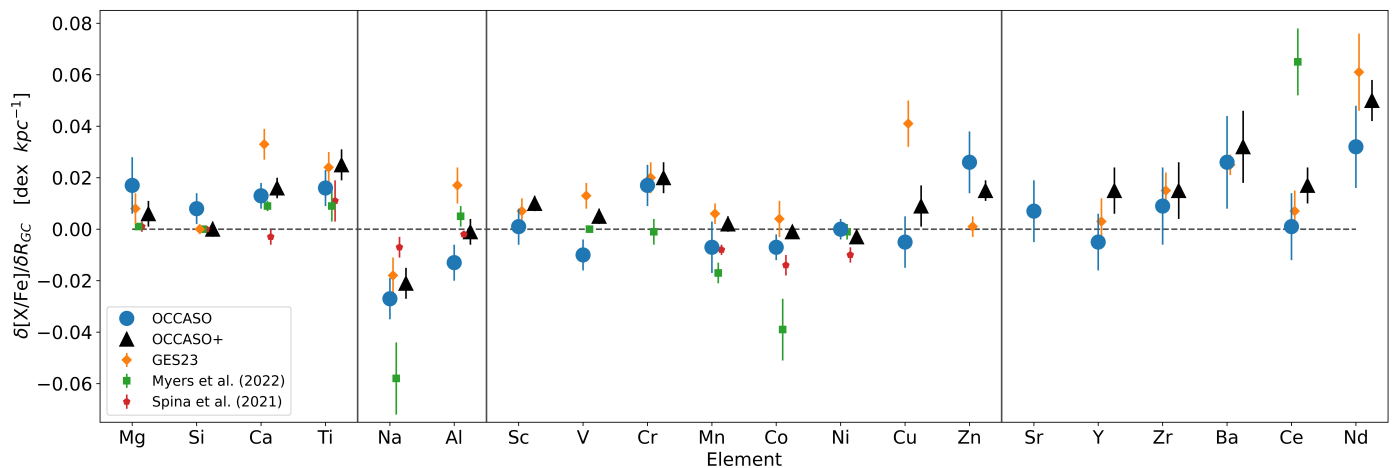


Fig. 16. Comparison of $[X/Fe]$ radial gradients with the literature.

Ga ago. The presence of OCs older than 1 Ga at more than 14 kpc, together with the appearance of the knee from this epoch, supports this hypothesis. The recent cepheid study by da Silva et al. (2023) shows signs of flattening in the outer disc. Given the youth of these stars, the presence of cepheids forming a plateau cannot be explained by radial migration processes. Further research is needed on both tracers in the outer disc.

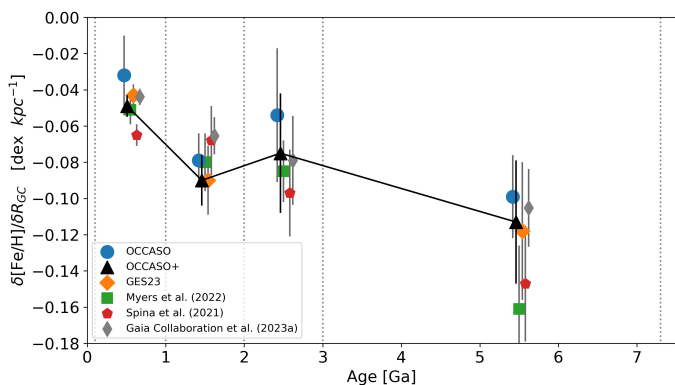


Fig. 17. Evolution of the $[Fe/H]$ radial gradient with age for the different samples analysed. The gradients are those measured inside the knee. The age position of each sample is slightly changed for clarity of the plot.

Figure 18 shows the change of $\delta[X/Fe]/\delta R_{GC}$ as a function of age of the OCCASO+ sample. Filled symbols represent the slopes coloured by the age range, and blue lines represent the gradient for all the OCs independently of age. In cases where we did not find a knee in the global analysis, we have analysed each age bin using clusters up to 16 kpc. Otherwise, in the cases where we found a knee, we evaluated the slope of the first line of the fit (m1 in Table 5). We recall that when separating the samples by age, the amount of OCs per bin is small, and therefore the differences might be dominated by small number statistics. In most of the cases, the values in each bin are around the global one, without a clear correlation with age. Therefore, for almost all elements, if there is gradient age dependence, it should be lower than our uncertainties. If we take as a reference the bin with the highest error, we can establish that the upper limit on the trend change is ~ 0.01 dex kpc^{-1} . This value is of the order of 6 times lower than the gradient change we find for $[Fe/H]$ indicating the absence of change with age of $\delta[X/Fe]/\delta R_{GC}$. Or, in other words, $\delta[X/H]/\delta R_{GC}$ changes with age essentially as

$\delta[Fe/H]/\delta R_{GC}$. However, there are hints of trend change for some elements. $[Mg/Fe]$ seems to show an increase in the gradient with age, while $[Ti/Fe]$ and $[Ni/Fe]$ appear to decrease. More OCs and a better distribution among the different age bins are needed to address this topic in more detail.

4.5. Azimuthal gradient

One interesting feature of the metallicity distribution of the OCs population as a function of Galactocentric radius is the large dispersion (>0.3 dex) observed at any position (Figs. 14 and 15). This dispersion cannot be explained by individual uncertainties and is usually attributed to the radial migration. During their lifetimes, stars, and OCs, can move from their birth Galactocentric radius due to the dynamical influence of non-axisymmetric structures in the Galaxy such as spiral arms (e.g., Sellwood & Binney 2002), the bar (e.g., Minchev & Famaey 2010) or minor satellites (e.g., Quillen et al. 2009). An alternative explanation is that the observed dispersion could be due to variations of the metal content with Galactic azimuth, as proposed by Friel (2013). Some evidence of abundance variations with the azimuth has been reported for Cepheids (Luck et al. 2006) and young OCs (Davies et al. 2009) but not for H II regions (Arellano-Córdova et al. 2020). However, the lack of OC samples covering a wide azimuthal range has hampered the investigation of this hypothesis.

We studied the same five samples analysed in the previous section in order to check the existence of an azimuthal gradient. For this purpose, we fit simultaneously the radial and azimuthal gradients with OCs separated in the same age bins used in the previous section. To do that, we fit a plane using the `scikit-spatial`² python package. The uncertainties are constrained by generating 1000 possible values for each cluster assuming a Gaussian distribution centred on the mean abundance, with a σ equal to its uncertainty. The resulting fits are listed in Table A.7 and shown in Fig. 19 in the two projections (R_{GC} , and azimuth Φ). We do not represent bins containing less than 10 OCs as we consider this to be insufficient statistics to conduct the study. Compared to Fig. 17 the evolution of the R_{GC} gradient (left panel) shows larger differences among samples, particularly in the oldest age bin, probably due to the additional dimension of the fit. In the case of OCCASO+ the obtained slopes are compatible with the results of Sect. 4.4. In the right panel of Fig. 19 we

² <https://scikit-spatial.readthedocs.io/en/stable/index.html>

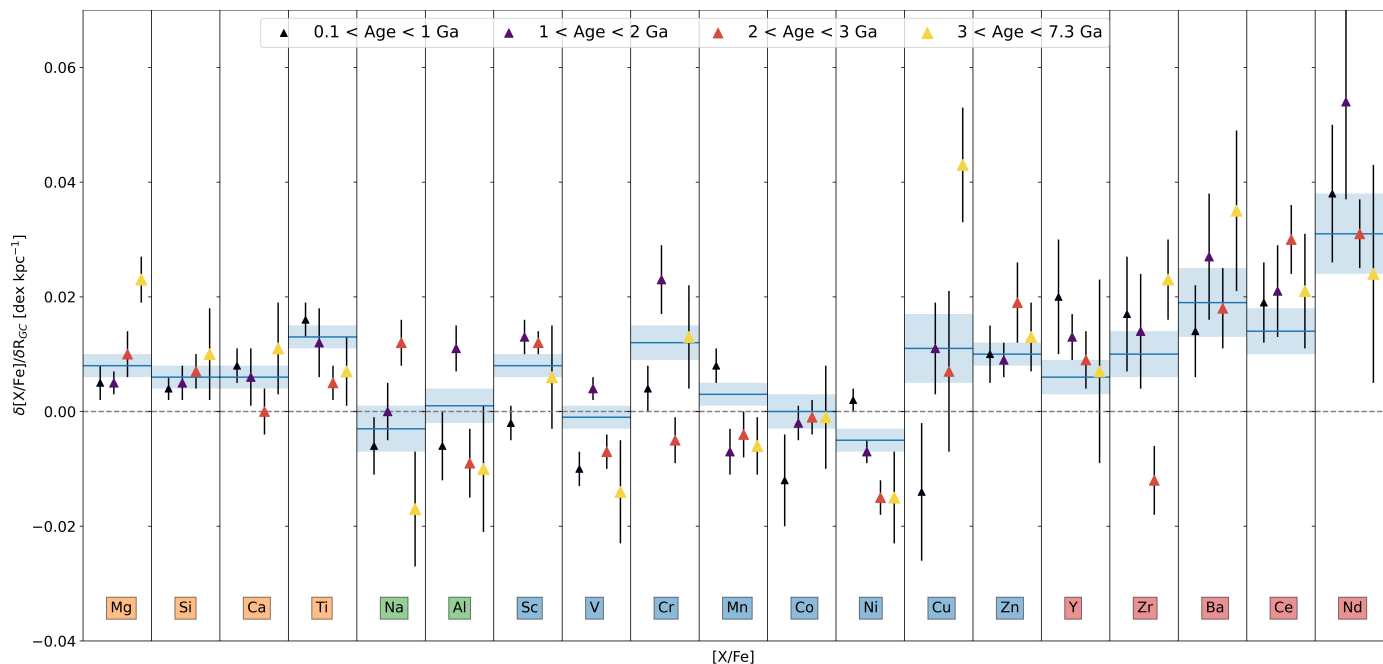


Fig. 18. Change of OCCASO+ [X/Fe] radial gradient in four age bins, depicted by the size and the colour of the markers. In each panel, age is growing towards the right. Blue horizontal lines represent the radial gradient for the whole age range, and the shadow area shows its dispersion. The table with the trends is available under request.

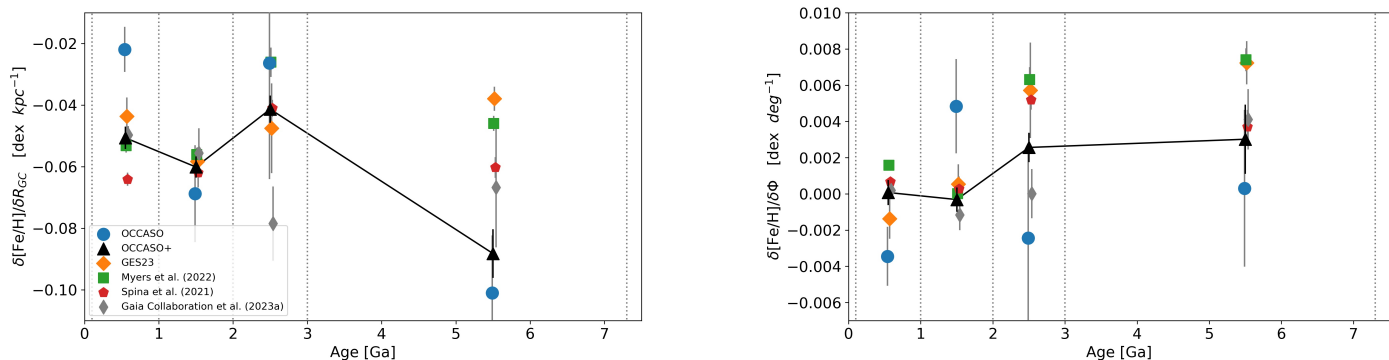


Fig. 19. Evolution with age of the [Fe/H] radial gradient (left) analysed at the same time as the azimuthal gradient (right). The age position of each sample is slightly changed for clarity of the plot.

show the evolution of the azimuthal gradient. The two youngest bins, in the OCCASO+ sample, do not show a dependence with azimuth, but there are hints of a positive trend in the oldest ones. This tendency also appears at GES23, Myers et al. (2022) and Spina et al. (2021) samples. (Gaia Collaboration et al. 2023a), shows a flat gradient in the third age bin and a positive gradient for the oldest OCs group. To extract clearer conclusions about the existence of an azimuthal variation, larger samples are needed.

4.6. Dependence with $|Z_{max}|$

Several studies have investigated the vertical distribution of abundance with respect to the distance from the Galactic plane (Z). A vertical gradient has been reported for field stars (e.g., Boeche et al. 2013; Gaia Collaboration et al. 2023a; Hawkins 2023) but not in OCs (e.g., Jacobson et al. 2011; Carrera & Pancino 2011; Carrera et al. 2019). Clusters move along their orbits; hence, here we consider the maximum height of a cluster ($|Z_{max}|$)

as a better tracer to perform this study. This orbital parameter has been computed in Paper IV. $|Z_{max}|$ is known to be correlated with OC age (Tarricq et al. 2021). This is usually attributed to the vertical heating of the disc, since OCs born in the thin disc, are scattered away from the mid-plane by non-axisymmetric components. This is coupled with the fact that the Galactic potential tends to disrupt OCs, having more chances to survive those that pass more time far away from the disc mid-plane.

We do not observe a vertical gradient with [Fe/H], in agreement with previous works. This could be because OCs cover a smaller range of vertical distances ($|Z_{max}| \leq 1.4$ kpc in our sample) compared to field stars. However, we did find positive $[X/Fe]-|Z_{max}|$ gradients for Mg, Ti, Al, and Ni, and negative gradients for Na, Sr, Y, Zr, Ba, and Nd. These trends are clearly associated with the dependence of [X/Fe] on age, as discussed in Sect. 4.2. When we remove the age dependence, the variations with vertical distance disappear.

5. Summary and Conclusions

In this work, we obtain high-resolution spectra for 194 stars, members of 36 open clusters. We used both equivalent widths and spectral synthesis methods to determine atmospheric parameters and LTE chemical abundances for 21 elements belonging to the main nucleosynthesis groups (α , odd-Z, Fe-peak, and neutron-capture elements). We also provide NLTE abundances for elements when corrections are available. Additionally, we construct the OCCASO+ sample by adding the abundances of other 63 clusters studied in similar conditions to ours: high-resolution ($R > 20\,000$) and at least four stars sampled in the red-clump region. Both samples are used to investigate abundance trends with R_{GC} , and their temporal evolution, azimuth and distance to the plane, from the orbital parameter $|Z_{max}|$, and the abundance dependence with age. The main results of our work are:

- Some of the studied elements show dependencies with age. [Mg/Fe] and [Si/Fe] show a positive trend towards older ages. Some clusters younger than 0.7 Ga show an unexpected enhancement in those elements. [Na/Fe] shows a decreasing trend until ~ 1.8 Ga and a plateau for older ages, while [Al/Fe] shows a mild positive trend. [Sc/Fe], [Ni/Fe], and [Cu/Fe] show significant positive trends, while [V/Fe], [Co/Fe] and [Zn/Fe] show negative trends. The neutron capture elements show negative gradients, those of [Zr/Fe] and [Ba/Fe] having a flattening at ages > 2.5 Ga.
- We find that the [X/Fe]-age trend of neutron-capture elements depends on their s-process contribution.
- There is a decreasing [Fe/H] radial gradient, and a flattening of the trend beyond 11.3 ± 0.8 kpc, the so-called knee shape. Inside the knee radius, the OCCASO and OCCASO+ samples show gradients of -0.06 ± 0.02 dex kpc^{-1} and -0.07 ± 0.01 dex kpc^{-1} , respectively. Outside the knee, the OCCASO+ sample shows a gradient of -0.03 ± 0.01 dex kpc^{-1} .
- The radial gradients of the other elements show different tendencies depending on the group to which they belong. α elements have a positive gradient, except [Si/Fe]. [Na/Fe] has a negative gradient, while [Al/Fe] show a flat one. Fe-peak elements have flat gradients, except for [Cr/Fe] and [Zn/Fe] that show positive trends. Neutron capture elements show different behaviours, having [Ba/Fe] and [Nd/Fe] the steepest positive trends.
- The [Fe/H] radial gradient shows a steepening with age that seems to be non-linear, since the second age bin ($1 > \text{age} > 2$ Ga) has a steeper gradient than expected considering the other age bins. We also find that the younger clusters (< 1 Ga) do not have the knee shape seen in the older ones. This suggests that the event that produced the knee occurred more than 1 Ga ago. This, together with the absence of young clusters at more than 14 kpc, supports the hypothesis that the knee shape was formed by outward radial migration.
- When examining the temporal evolution of [X/Fe] radial gradient, we generally observe that the trend within each age bin follows the overall trend calculated using all the open clusters. Hence, we do not observe a clear correlation between these trends and the age bin. If there was any evolution of the gradient over time, it would be smaller than our uncertainties. As a result, we can determine an upper limit of ~ 0.01 dex kpc^{-1} for the extent of their change with age. This is, in general, a negligible value of change with age for [X/Fe] gradient. Nevertheless, there are hints that certain elements exhibit an evolution of their radial gradients. Mg appears to

show an increase in the gradient with age, while Ti and Ni seem to display a decrease.

- One feature of the [Fe/H] radial dependence is the large dispersion (> 0.3 dex) observed at any position. That is widely attributed to the radial migration, but the observed dispersion could be due to variations of the metal content with Galactic azimuth. We study the existence of the azimuthal gradient by splitting the sample into age bins. We do not find any dependence on azimuth for clusters with ages between 0.1 and 2 Ga. However, we observe hints of a positive trend for open clusters with ages between 2 and 7.3 Ga.
- We find $\delta[X/Fe]/\delta|Z_{max}|$ gradients that are mostly due to the trends with age. They disappear once the age dependence is subtracted.

Acknowledgements. This work was supported by the MINECO (Spanish Ministry of Economy, Industry and Competitiveness) through grant ESP2016-80079-C2-1-R (MINECO/FEDER, UE) and by the Spanish MICIN/AEI/10.13039/501100011033 and by "ERDF A way of making Europe" by the "European Union" through grants RTI2018-095076-B-C21 and PID2021-122842OB-C21, and the Institute of Cosmos Sciences University of Barcelona (ICCUB, Unidad de Excelencia 'María de Maeztu') through grant CEX2019-000918-M. LC acknowledges the grant RYC2021-033762-I funded by MICIN/AEI/10.13039/501100011033 and by the European Union NextGenerationEU/PRTR. GT, ES, and AD acknowledge funding from the Lithuanian Science Council (LMTLT, grant No. P-MIP-23-24). Based on observations made with the Nordic Optical Telescope, owned in collaboration by the University of Turku and Aarhus University, and operated jointly by Aarhus University, the University of Turku and the University of Oslo, representing Denmark, Finland and Norway, the University of Iceland and Stockholm University at the Observatorio del Roque de los Muchachos, La Palma, Spain, of the Instituto de Astrofísica de Canarias. Based on observations made with the Mercator Telescope, operated on the island of La Palma by the Flemish Community, at the Spanish Observatorio del Roque de los Muchachos of the Instituto de Astrofísica de Canarias. Based on observations obtained with the HERMES spectrograph, which is supported by the Research Foundation - Flanders (FWO), Belgium, the Research Council of KU Leuven, Belgium, the Fonds National de la Recherche Scientifique (F.R.S.-FNRS), Belgium, the Royal Observatory of Belgium, the Observatoire de Genève, Switzerland and the Thüringer Landessternwarte Tautenburg, Germany. Based on observations collected at Centro Astronómico Hispano en Andalucía (CAHA) at Calar Alto, operated jointly by Instituto de Astrofísica de Andalucía (CSIC) and Junta de Andalucía. This research has made use of NASA's Astrophysics Data System Bibliographic Services.

References

- Abdurro'uf, Accetta, K., Aerts, C., et al. 2022, *ApJS*, 259, 35
 Aceituno, J., Sánchez, S. F., Grupp, F., et al. 2013, *A&A*, 552, A31
 Adibekyan, V. Z., Sousa, S. G., Santos, N. C., et al. 2012, *A&A*, 545, A32
 Anders, F., Chiappini, C., Minchev, I., et al. 2017, *A&A*, 600, A70
 Anders, F., Gispert, P., Ratcliffe, B., et al. 2023, *A&A*, 678, A158
 Arellano-Córdova, K. Z., Esteban, C., García-Rojas, J., & Méndez-Delgado, J. E. 2020, *MNRAS*, 496, 1051
 Asplund, M., Grevesse, N., Sauval, A. J., & Scott, P. 2009, *ARA&A*, 47, 481
 Bailer, D. S., Rood, R. T., Bania, T. M., & Anderson, L. D. 2011, *ApJ*, 738, 27
 Bergemann, M. 2011, *MNRAS*, 413, 2184
 Bergemann, M. & Cescutti, G. 2010, *A&A*, 522, A9
 Bergemann, M. & Gehren, T. 2008, *A&A*, 492, 823
 Bergemann, M., Kudritzki, R.-P., Gazak, Z., Davies, B., & Plez, B. 2015, *ApJ*, 804, 113
 Bergemann, M., Kudritzki, R.-P., Würl, M., et al. 2013, *ApJ*, 764, 115
 Bergemann, M., Lind, K., Collet, R., Magic, Z., & Asplund, M. 2012, *MNRAS*, 427, 27
 Bergemann, M., Pickering, J. C., & Gehren, T. 2010, *MNRAS*, 401, 1334
 Bisterzo, S., Pompeia, L., Gallino, R., et al. 2005, *Nucl. Phys. A*, 758, 284
 Bisterzo, S., Travaglio, C., Gallino, R., Wiescher, M., & Käppeler, F. 2014, *ApJ*, 787, 10
 Bisterzo, S., Travaglio, C., Wiescher, M., Käppeler, F., & Gallino, R. 2017, *ApJ*, 835, 97
 Blanco-Cuaresma, S. 2019, *MNRAS*, 486, 2075
 Blanco-Cuaresma, S., Soubiran, C., Heiter, U., & Jofré, P. 2014a, *A&A*, 569, A111

- Blanco-Cuaresma, S., Soubiran, C., Jofré, P., & Heiter, U. 2014b, *A&A*, 566, A98
- Boeche, C., Siebert, A., Piffl, T., et al. 2014, *A&A*, 568, A71
- Boeche, C., Siebert, A., Piffl, T., et al. 2013, *A&A*, 559, A59
- Bragaglia, A., Sestito, P., Villanova, S., et al. 2008, *A&A*, 480, 79
- Bragança, G. A., Daflon, S., Lanz, T., et al. 2019, *A&A*, 625, A120
- Buder, S., Sharma, S., Kos, J., et al. 2021, *MNRAS*, 506, 150
- Cantat-Gaudin, T., Anders, F., Castro-Ginard, A., et al. 2020, *A&A*, 640, A1
- Cantat-Gaudin, T., Vallenari, A., Zaggia, S., et al. 2014, *A&A*, 569, A17
- Carrera, R., Bragaglia, A., Cantat-Gaudin, T., et al. 2019, *A&A*, 623, A80
- Carrera, R., Casamiquela, L., Carbajo-Hijarrubia, J., et al. 2022, *A&A*, 658, A14
- Carrera, R. & Pancino, E. 2011, *A&A*, 535, A30
- Casagrande, L., Schönrich, R., Asplund, M., et al. 2011, *A&A*, 530, A138
- Casamiquela, L., Blanco-Cuaresma, S., Carrera, R., et al. 2019, *MNRAS*, 490, 1821
- Casamiquela, L., Carrera, R., Balaguer-Núñez, L., et al. 2018, *A&A*, 610, A66
- Casamiquela, L., Carrera, R., Blanco-Cuaresma, S., et al. 2017, *MNRAS*, 470, 4363
- Casamiquela, L., Carrera, R., Jordi, C., et al. 2016, *MNRAS*, 458, 3150
- Casamiquela, L., Soubiran, C., Jofré, P., et al. 2021, *A&A*, 652, A25
- Casamiquela, L., Tarricq, Y., Soubiran, C., et al. 2020, *A&A*, 635, A8
- Cristallo, S., Straniero, O., Gallino, R., et al. 2009, *ApJ*, 696, 797
- Cristallo, S., Straniero, O., Piersanti, L., & Gobrecht, D. 2015, *ApJS*, 219, 40
- da Silva, R., Crestani, J., Bono, G., et al. 2022, *A&A*, 661, A104
- da Silva, R., D'Orazi, V., Palla, M., et al. 2023, *A&A*, 678, A195
- Daflon, S. & Cunha, K. 2004, *ApJ*, 617, 1115
- Davies, B., Origlia, L., Kudritzki, R.-P., et al. 2009, *ApJ*, 696, 2014
- De Silva, G. M., Freeman, K. C., Bland-Hawthorn, J., et al. 2015, *MNRAS*, 449, 2604
- Dekker, H., D'Odorico, S., Kaufer, A., Delabre, B., & Kotzłowski, H. 2000, in *Society of Photo-Optical Instrumentation Engineers (SPIE) Conference Series*, Vol. 4008, *Optical and IR Telescope Instrumentation and Detectors*, ed. M. Iye & A. F. Moorwood, 534–545
- Delgado Mena, E., Moya, A., Adibekyan, V., et al. 2019, *A&A*, 624, A78
- Delgado Mena, E., Tsantaki, M., Adibekyan, V. Z., et al. 2017, *A&A*, 606, A94
- Donati, P., Cocozza, G., Bragaglia, A., et al. 2015, *MNRAS*, 446, 1411
- Donor, J., Frinchaboy, P. M., Cunha, K., et al. 2020, *AJ*, 159, 199
- D'Orazi, V., Magrini, L., Randich, S., et al. 2009, *ApJ*, 693, L31
- Foreman-Mackey, D., Conley, A., Meierjürgen Farr, W., et al. 2013, emcee: The MCMC Hammer, *Astrophysics Source Code Library*, record ascl:1303.002
- Friel, E. D. 2013, in *Planets, Stars and Stellar Systems. Volume 5: Galactic Structure and Stellar Populations*, ed. T. D. Oswalt & G. Gilmore, Vol. 5, 347
- Friel, E. D., Janes, K. A., Tavaréz, M., et al. 2002, *AJ*, 124, 2693
- Gaia Collaboration, Recio-Blanco, A., Kordopatis, G., et al. 2023a, *A&A*, 674, A38
- Gaia Collaboration, Vallenari, A., Brown, A. G. A., et al. 2023b, *A&A*, 674, A1
- Gaia Collaboration, Brown, A. G. A., Vallenari, A., et al. 2018, *A&A*, 616, A1
- Gaia Collaboration, Prusti, T., de Bruijne, J. H. J., et al. 2016, *A&A*, 595, A1
- Gallino, R., Arlandini, C., Busso, M., et al. 1998, *ApJ*, 497, 388
- Gallino, R., Bisterzo, S., Straniero, O., Ivans, I. I., & Käppeler, F. 2006, *Mem. Soc. Astron. Italiana*, 77, 786
- Genovali, K., Lemasle, B., Bono, G., et al. 2014, *A&A*, 566, A37
- Gilmore, G., Randich, S., Asplund, M., et al. 2012, *The Messenger*, 147, 25
- Gray, R. O. & Corbally, C. J. 1994, *AJ*, 107, 742
- Grevesse, N., Asplund, M., & Sauval, A. J. 2007, *Space Sci. Rev.*, 130, 105
- Gustafsson, B., Edvardsson, B., Eriksson, K., et al. 2008, *A&A*, 486, 951
- Hawkins, K. 2023, *MNRAS*, 525, 3318
- Heiter, U., Jofré, P., Gustafsson, B., et al. 2015, *A&A*, 582, A49
- Heiter, U., Lind, K., Bergemann, M., et al. 2021, *A&A*, 645, A106
- Jacobson, H. R., Friel, E. D., & Pilachowski, C. A. 2011, *AJ*, 141, 58
- Janes, K. A. 1979, *ApJS*, 39, 135
- Kajino, T., Aoki, W., Balantekin, A. B., et al. 2019, *Progress in Particle and Nuclear Physics*, 107, 109
- Karakas, A. I. & Lattanzio, J. C. 2014, *PASA*, 31, e030
- Kobayashi, C., Karakas, A. I., & Lugaro, M. 2020, *ApJ*, 900, 179
- Korotin, S. A., Andrievsky, S. M., Hansen, C. J., et al. 2015, *A&A*, 581, A70
- Kurucz, R. L. 2005, *Memorie della Societa Astronomica Italiana Supplementi*, 8, 14
- Lagarde, N., Decressin, T., Charbonnel, C., et al. 2012, *A&A*, 543, A108
- Lillo-Box, J., Aceituno, J., Pedraz, S., et al. 2020, *MNRAS*, 491, 4496
- Lind, K., Asplund, M., Barklem, P. S., & Belyaev, A. K. 2011, *A&A*, 528, A103
- Luck, R. E. 2018, *AJ*, 156, 171
- Luck, R. E., Kovtyukh, V. V., & Andrievsky, S. M. 2006, *AJ*, 132, 902
- Maciel, W. J., Quireza, C., & Costa, R. D. D. 2007, *A&A*, 463, L13
- Magrini, L., Randich, S., Kordopatis, G., et al. 2017, *A&A*, 603, A2
- Magrini, L., Randich, S., Romano, D., et al. 2014, *A&A*, 563, A44
- Magrini, L., Sestito, P., Randich, S., & Galli, D. 2009, *A&A*, 494, 95
- Magrini, L., Viscasillas Vázquez, C., Spina, L., et al. 2023, *A&A*, 669, A119
- Majewski, S. R., Schiavon, R. P., Frinchaboy, P. M., et al. 2017, *AJ*, 154, 94
- Mashonkina, L., Korn, A. J., & Przybilla, N. 2007, *A&A*, 461, 261
- Méndez-Delgado, J. E., Amayo, A., Arellano-Córdova, K. Z., et al. 2022, *MNRAS*, 510, 4436
- Mikolaitis, Š., Drzdauskas, A., Minkevičiūtė, R., et al. 2019, *A&A*, 628, A49
- Minchev, I. & Famaey, B. 2010, in *EAS Publications Series*, Vol. 45, *EAS Publications Series*, 299–302
- Minniti, J. H., Sbordone, L., Rojas-Arriagada, A., et al. 2020, *A&A*, 640, A92
- Mucciarelli, A., Pancino, E., Lovisi, L., Ferraro, F. R., & Lapenna, E. 2013, *ApJ*, 766, 78
- Myers, N., Donor, J., Spoo, T., et al. 2022, *AJ*, 164, 85
- Netopil, M., Oralhan, İ. A., Çakmak, H., Michel, R., & Karataş, Y. 2022, *MNRAS*, 509, 421
- Netopil, M., Paunzen, E., Heiter, U., & Soubiran, C. 2016, *A&A*, 585, A150
- Pancino, E., Carrera, R., Rossetti, E., & Gallart, C. 2010, *A&A*, 511, A56
- Plez, B. 2012, *Turbospectrum: Code for spectral synthesis*, *Astrophysics Source Code Library*, record ascl:1205.004
- Prantzos, N., Abia, C., Cristallo, S., Limongi, M., & Chieffi, A. 2020, *MNRAS*, 491, 1832
- Prantzos, N., Abia, C., Limongi, M., Chieffi, A., & Cristallo, S. 2018, *MNRAS*, 476, 3432
- Quillen, A. C., Minchev, I., Bland-Hawthorn, J., & Haywood, M. 2009, *MNRAS*, 397, 1599
- Randich, S., Gilmore, G., Magrini, L., et al. 2022, *A&A*, 666, A121
- Raskin, G., van Winckel, H., Hensberge, H., et al. 2011, *A&A*, 526, A69
- Recio-Blanco, A., de Laverny, P., Palicio, P. A., et al. 2023, *A&A*, 674, A29
- Reddy, A. B. S. & Lambert, D. L. 2017, *ApJ*, 845, 151
- Roesselein, M., Wolf, M., Wampfler, B., & Wegscheider, W. 2007, *Springer*, 12, 495
- Romano, D. & Matteucci, F. 2007, *MNRAS*, 378, L59
- Sales-Silva, J. V., Daflon, S., Cunha, K., et al. 2022, *ApJ*, 926, 154
- Sellwood, J. A. & Binney, J. J. 2002, *MNRAS*, 336, 785
- Sestito, P., Bragaglia, A., Randich, S., et al. 2008, *A&A*, 488, 943
- Smiljanic, R., Korn, A. J., Bergemann, M., et al. 2014, *A&A*, 570, A122
- Smiljanic, R., Romano, D., Bragaglia, A., et al. 2016, *A&A*, 589, A115
- Spina, L., Magrini, L., & Cunha, K. 2022, *Universe*, 8, 87
- Spina, L., Meléndez, J., Karakas, A. I., et al. 2016, *A&A*, 593, A125
- Spina, L., Nordlander, T., Casey, A. R., et al. 2020, *ApJ*, 895, 52
- Spina, L., Ting, Y. S., De Silva, G. M., et al. 2021, *MNRAS*, 503, 3279
- Stanghellini, L. & Haywood, M. 2018, *ApJ*, 862, 45
- Stetson, P. B. & Pancino, E. 2008, *PASP*, 120, 1332
- Tarricq, Y., Soubiran, C., Casamiquela, L., et al. 2021, *A&A*, 647, A19
- Tautvaišienė, G., Viscasillas Vázquez, C., Mikolaitis, Š., et al. 2021, *A&A*, 649, A126
- Telting, J. H., Avila, G., Buchhave, L., et al. 2014, *Astronomische Nachrichten*, 335, 41
- Thygesen, A. O., Frandsen, S., Bruntt, H., et al. 2012, *A&A*, 543, A160
- Viscasillas Vázquez, C., Magrini, L., Casali, G., et al. 2022, *A&A*, 660, A135
- Yong, D., Carney, B. W., & Friel, E. D. 2012, *AJ*, 144, 95
- Zhang, R., Lucatello, S., Bragaglia, A., et al. 2021, *A&A*, 654, A77

Appendix A: Complementary tables and figures

Table A.1. First rows of the table with the line list for EW. The complete table is available at the CDS.

Wavelength (nm)	Element
480.288	FeI
480.8148	FeI
480.9938	FeI
481.0528	ZnI
481.1983	NiI
481.4590	NiI
482.3463	MnI
482.3483	MnI
482.3495	MnI
482.3508	MnI

Table A.2. First rows of the table with the line list for SS. The complete table is available at the CDS.

Wavelength (nm)	Element
480.1025	CrI
480.288	FeI
480.8148	FeI
481.0528	ZnI
481.1983	NiI
481.4591	NiI
482.352	MnI
483.2426	V I
486.9463	FeI
487.5493	TiI

Table A.3. $[X/Fe]$ abundance dependence with age of the samples OCCASO and OCCASO+ and its uncertainties computed in Sect. 4.2. N and ρ are the number of OCs and the Spearman correlation coefficient, respectively.

Element	OCCASO			OCCASO+		
	$\delta[X/Fe]/\delta Age$ [dex Ga ⁻¹]	N	ρ	$\delta[X/Fe]/\delta Age$ [dex Ga ⁻¹]	N	ρ
Mg	0.009±0.007	36	0.48	0.012±0.009	99	0.37
Si	0.012±0.008	36	0.64	0.011±0.003	99	0.41
Ca	0.008±0.005	36	0.15	-0.001±0.001	99	0.05
Ti	0.009±0.005	36	0.66	0.005±0.003	99	0.37
Na	-0.03±0.013	36	-0.11	-0.005±0.003	99	-0.12
Al	0.02±0.011	36	0.61	0.003±0.002	99	0.49
Sc	-0.005±0.004	36	-0.43	0.017±0.005	76	-0.21
V	0.01±0.005	36	0.62	0.009±0.004	99	0.18
Cr	0.018±0.004	36	0.63	0.002±0.002	99	0.21
Mn	0.003±0.007	36	0.25	0.005±0.003	99	0.21
Co	0.007±0.005	36	0.29	0.01±0.004	99	0.32
Ni	0.026±0.006	36	0.77	0.027±0.005	99	0.54
Cu	0.016±0.008	36	0.52	0.024±0.006	78	0.38
Zn	0.02±0.012	32	0.12	0.01±0.004	76	0.21
Sr	-0.07±0.008	35	-0.77	–	–	–
Y	-0.022±0.012	36	-0.80	-0.011±0.008	80	-0.35
Zr	-0.027±0.013	35	-0.7	-0.023±0.007	78	-0.38
Ba	-0.066±0.007	36	-0.76	-0.058±0.011	80	-0.48
Ce	-0.044±0.015	36	-0.69	-0.022±0.008	94	-0.47
Nd	-0.032±0.011	36	-0.69	-0.016±0.009	80	-0.11

Table A.4. Stellar parameters and chemical abundances for the 194 stars in this work. Here only a sample of rows and columns is shown. The complete table with all the atmospheric parameters and the 21 elements computed by EW and SS methods is available at the CDS.

Cluster	source id <i>Gaia</i> DR3	T_{eff} (K)	log g	GALAF	[Fe/H] _{EW}	[Mg/Fe] _{SS}	[Si/Fe] _{EW}	[Ca/Fe] _{SS}	[Ti/Fe] _{EW}
NGC1907	183263711899696768	5215±55	2.77±0.10	1	-0.05±0.01	0.02±0.03	0.11±0.03	0.06±0.04	0.10±0.03
NGC1907	183263097725025024	5030±55	2.60±0.09	1	-0.03±0.01	-0.05±0.03	0.08±0.03	0.04±0.03	0.03±0.03
NGC1907	183263127784145280	5201±43	2.67±0.12	1	-0.06±0.01	0.02±0.03	0.072±0.03	0.04±0.03	0.03±0.03
NGC1907	183263127784146176	5273±55	3.04±0.11	4	-0.03±0.01	0.03±0.04	0.06±0.04	-0.01±0.04	0.11±0.03
NGC2099	3451181873619100160	5079±55	2.73±0.12	1	0.07±0.01	-0.07±0.02	0.13±0.04	0.01±0.03	-0.01±0.03
NGC2099	3451181766240577024	5047±40	2.60±0.08	1	0.04±0.01	-0.07±0.02	0.08±0.02	-0.01±0.03	0.00±0.03
NGC2099	3451180602308805120	5104±40	2.78±0.09	1	0.06±0.01	-0.07±0.02	0.05±0.04	0.02±0.03	0.01±0.03
NGC2099	3451181216484770432	4975±41	2.54±0.10	1	0.03±0.01	-0.07±0.03	0.06±0.03	-0.01±0.03	0.00±0.03
NGC2099	3451181667460701440	5115±43	2.78±0.08	1	0.01±0.01	-0.09±0.03	0.12±0.04	0.01±0.03	0.00±0.03
NGC2099	3451179949473813376	5052±46	2.61±0.06	4	0.06±0.01	-0.05±0.03	0.08±0.03	0.01±0.03	0.03±0.03
NGC2099	3451201458669932032	5065±45	2.68±0.07	1	0.06±0.01	-0.07±0.02	0.09±0.02	-0.01±0.03	0.04±0.03

Notes. GALAF is a quality flag assigned to GALA values derived in the study of how the initial guesses of atmospheric parameters affect their derivation (see Sect. 2.2.2).

Table A.5. Comparison of radial gradients between OCCASO, OCCASO+ and the literature reanalysis of Sect. 4.3.

[X/Fe]	Group	OCCASO $\delta[X/Fe]/\delta R_{GC}$ [dex kpc ⁻¹]	OCCASO+ $\delta[X/Fe]/\delta R_{GC}$ [dex kpc ⁻¹]	GES23 $\delta[X/Fe]/\delta R_{GC}$ [dex kpc ⁻¹]	Myers et al. (2022) $\delta[X/Fe]/\delta R_{GC}$ [dex kpc ⁻¹]	Spina et al. (2021) $\delta[X/Fe]/\delta R_{GC}$ [dex kpc ⁻¹]
Mg	α	0.017±0.011	0.006±0.005	0.008±0.006	0.001±0.001	0.001±0.002
Si	α	0.008±0.006	0.000±0.003	0.000±0.001	-0.0±0.001	0.0±0.001
Ca	α	0.013±0.005	0.016±0.004	0.033±0.006	0.009±0.002	-0.003±0.003
Ti	α	0.016±0.007	0.025±0.006	0.024±0.006	0.009±0.006	0.011±0.008
Na	Odd-Z	-0.027±0.008	-0.021±0.006	-0.018±0.007	-0.058±0.014	-0.007±0.004
Al	Odd-Z	-0.013±0.007	-0.001±0.005	0.017±0.007	0.005±0.004	-0.002±0.001
Sc	Fe-peak	0.001±0.007	0.01±0.003	0.007±0.005		
V	Fe-peak	-0.01±0.006	0.005±0.003	0.013±0.005	-0.0±0.001	
Cr	Fe-peak	0.017±0.008	0.02±0.006	0.020±0.005	-0.001±0.005	
Mn	Fe-peak	-0.007±0.010	0.002±0.003	0.006±0.005	-0.017±0.004	-0.008±0.002
Co	Fe-peak	-0.007±0.005	-0.001±0.002	0.003±0.007	-0.039±0.012	-0.014±0.004
Ni	Fe-peak	0.000±0.004	-0.003±0.002	-0.001±0.005	-0.001±0.003	-0.01±0.003
Cu	Fe-peak	-0.005±0.010	0.009±0.008	0.041±0.009		
Zn	Fe-peak	0.026±0.012	0.015±0.004	0.001±0.004		
Sr	n-capture	0.007±0.012				
Y	n-capture	-0.005±0.011	0.015±0.009	0.003±0.009		
Zr	n-capture	0.009±0.015	0.015±0.011	0.015±0.007		
Ba	n-capture	0.026±0.018	0.032±0.014	0.025±0.007		
Ce	n-capture	0.001±0.013	0.017±0.007	0.007±0.008	0.065±0.013	
Nd	n-capture	0.032±0.016	0.05±0.008	0.061±0.015		

Table A.6. [X/Fe] radial gradients studied through MCMC at Sect. 4.3 in the OCCASO+ sample. The columns b1 and m1 are the y-intercept and slope of the first line fitted, respectively. The column m2 is the slope of the second line. The position of the knee, the number of OCs and Spearman correlation coefficient are shown in the last columns.

Element	b1 [dex]	m1 [dex kpc ⁻¹]	m2 [dex kpc ⁻¹]	Knee [kpc]	N	Spearman
Mg	-0.118±0.021	0.008±0.002			99	0.29
Si	0.029±0.018	0.005±0.002			99	0.21
Ca	-0.07±0.022	0.008±0.002			99	0.42
Ti	-0.145±0.047	0.019±0.006	-0.003±0.009	10.7±1.1	99	0.40
Na	0.287±0.082	-0.026±0.01	0.015±0.008	9.9±0.8	99	-0.28
Al	-0.034±0.029	0.005±0.003			99	0.19
Sc	0.001±0.019	0.008±0.002			76	0.38
V	0.02±0.022	-0.002±0.002			99	0.09
Cr	-0.246±0.058	0.029±0.007	-0.008±0.005	9.5±0.5	99	0.33
Mn	-0.146±0.019	0.003±0.002			99	0.04
Co	0.019±0.027	0.002±0.003			99	0.11
Ni	0.008±0.018	-0.003±0.002			99	-0.11
Cu	-0.235±0.054	0.003±0.006			78	0.13
Zn	-0.152±0.021	0.01±0.002			76	0.54
Y	-0.129±0.037	0.011±0.004			80	0.38
Zr	-0.353±0.079	0.038±0.01	-0.02±0.007	9.6±0.4	78	0.18
Ba	-0.321±0.111	0.036±0.014	-0.016±0.018	10.3±1.2	80	0.25
Ce	-0.107±0.075	0.027±0.009	0.006±0.012	10.7±0.9	94	0.36
Nd	-0.382±0.074	0.049±0.009	0.016±0.016	10.7±1.3	80	0.71

Table A.7. Change with age of the [Fe/H] radial and azimuthal gradients studied with a multilinear regression at Sect. 4.5. We analyse the OCCASO and OCCASO+ samples and reanalyse the others. Number of OCs and Spearman correlation coefficient (sixth and seventh columns).

Sample	Age bin [Ga]	Radial gradient	Radial and Azimuthal Gradients		
		$\delta[\text{Fe}/\text{H}]/\delta R_{\text{GC}}$ [dex kpc ⁻¹]	$\delta[\text{Fe}/\text{H}]/\delta\Phi$ [dex deg ⁻¹]	N	Spearman
OCCASO	0.1 - 1	-0.022±0.007	-0.0034±0.0016	15	0.33
OCCASO	1 - 2	-0.069±0.016	0.0048±0.0026	11	0.83
OCCASO	2 - 3	-0.026±0.038	-0.0024±0.0049	4	0.34
OCCASO	3 - 7.3	-0.101±0.019	0.0003±0.0043	5	0.87
OCCASO+	0.1 - 1	-0.051±0.004	0.0001±0.0007	39	0.79
OCCASO+	1 - 2	-0.060±0.004	-0.0003±0.0007	29	0.87
OCCASO+	2 - 3	-0.041±0.004	0.0026±0.0008	14	0.92
OCCASO+	3 - 7.3	-0.088±0.008	0.003±0.0019	15	0.83
Myers et al. (2022)	0.1 - 1	-0.053±0.002	0.0016±0.0002	39	0.74
Myers et al. (2022)	1 - 2	-0.056±0.002	0.0000±0.0004	20	0.91
Myers et al. (2022)	2 - 3	-0.026±0.005	0.0063±0.0007	11	0.92
Myers et al. (2022)	3 - 7.3	-0.046±0.002	0.0074±0.0006	12	0.84
Spina et al. (2021)	0.1 - 1	-0.064±0.002	0.0007±0.0002	57	0.80
Spina et al. (2021)	1 - 2	-0.062±0.005	0.0003±0.0007	22	0.77
Spina et al. (2021)	2 - 3	-0.041±0.003	0.0052±0.0005	10	0.97
Spina et al. (2021)	3 - 7.3	-0.060±0.003	0.0037±0.0009	16	0.78
GES23	0.1 - 1	-0.044±0.006	-0.0014±0.0011	23	0.76
GES23	1 - 2	-0.058±0.005	0.0005±0.0011	17	0.88
GES23	2 - 3	-0.048±0.015	0.0057±0.0026	7	0.86
GES23	3 - 7.3	-0.038±0.004	0.0072±0.0012	12	0.77
Gaia DR3	0.1 - 1	-0.050±0.003	0.0002±0.0004	303	0.43
Gaia DR3	1 - 2	-0.056±0.008	-0.0012±0.0008	48	0.52
Gaia DR3	2 - 3	-0.079±0.012	0.0000±0.0014	25	0.57
Gaia DR3	3 - 7.3	-0.067±0.019	0.0041±0.0017	13	0.71

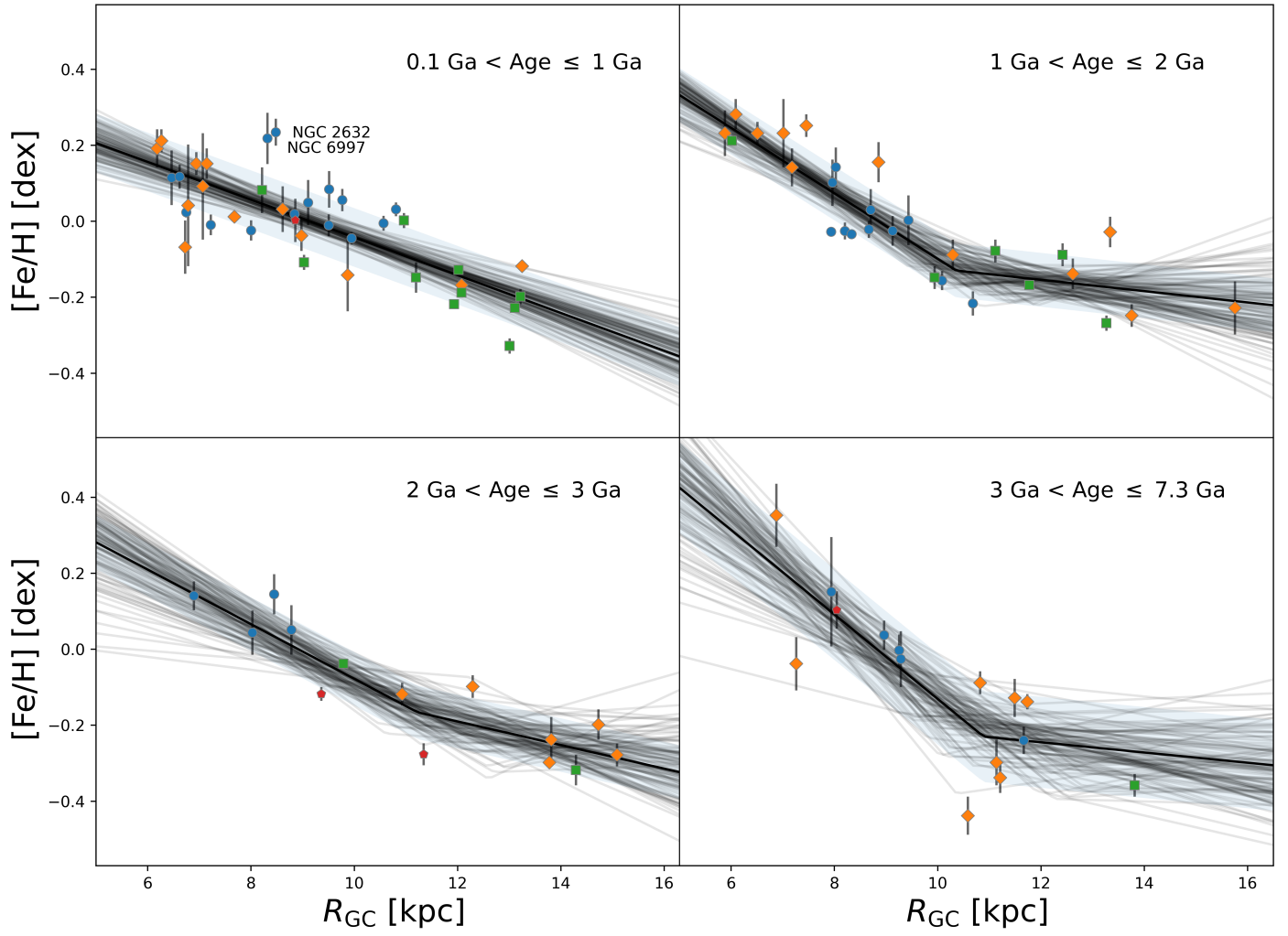


Fig. A.1. $[Fe/H]$ versus Galactocentric radius for OCCASO+ sample separated in four age bins 0.1-1, 1-2, 2-3, >3 Ga. The different surveys are colour-coded as in Fig. 1. The grey vertical lines represent the uncertainties, and the black line is our best fit.

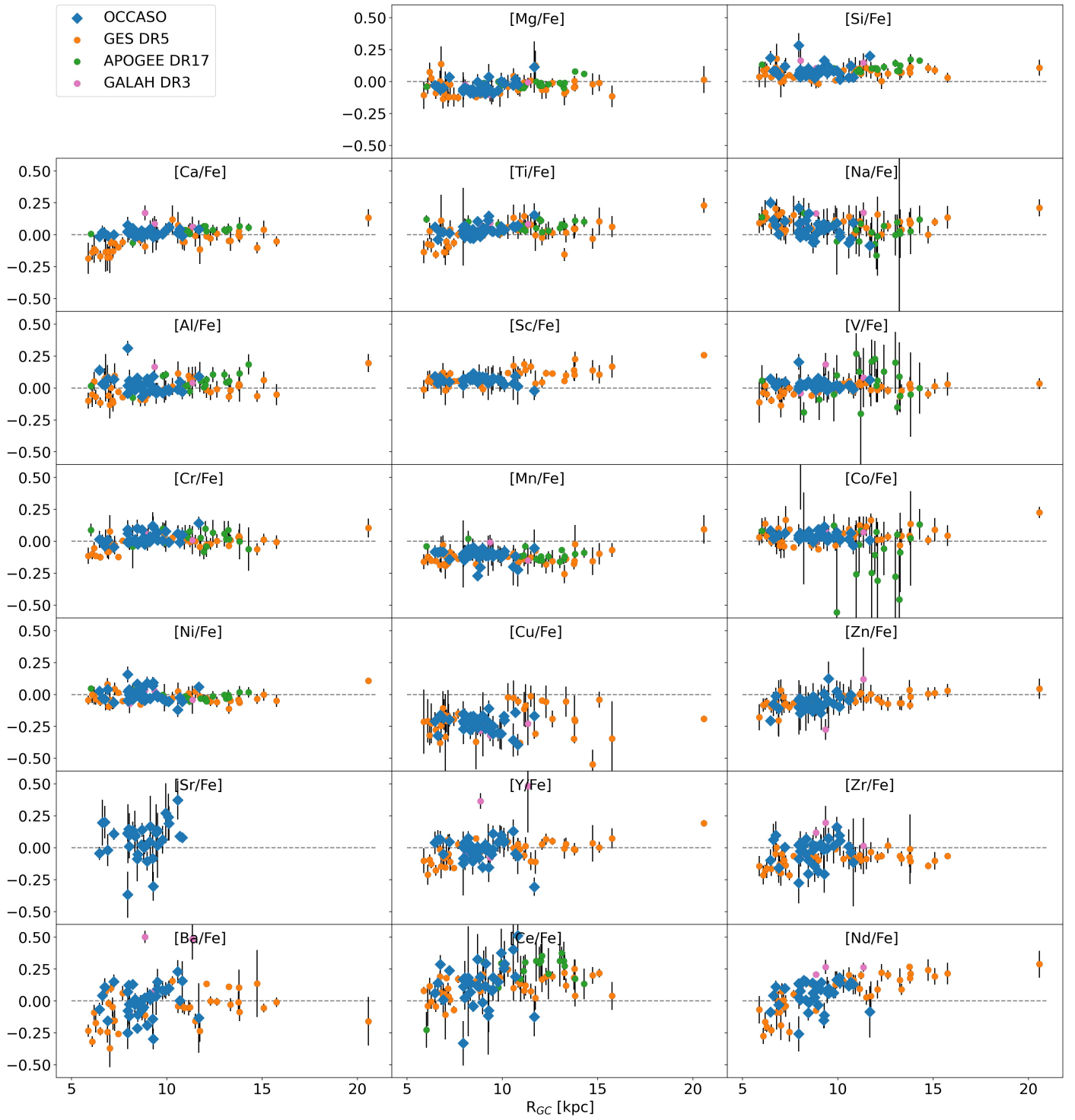


Fig. A.2. Dependence of $[X/Fe]$ on Galactocentric radius for the clusters in the OCCASO+ sample. The original sources of the abundances are indicated with different symbols and colours.

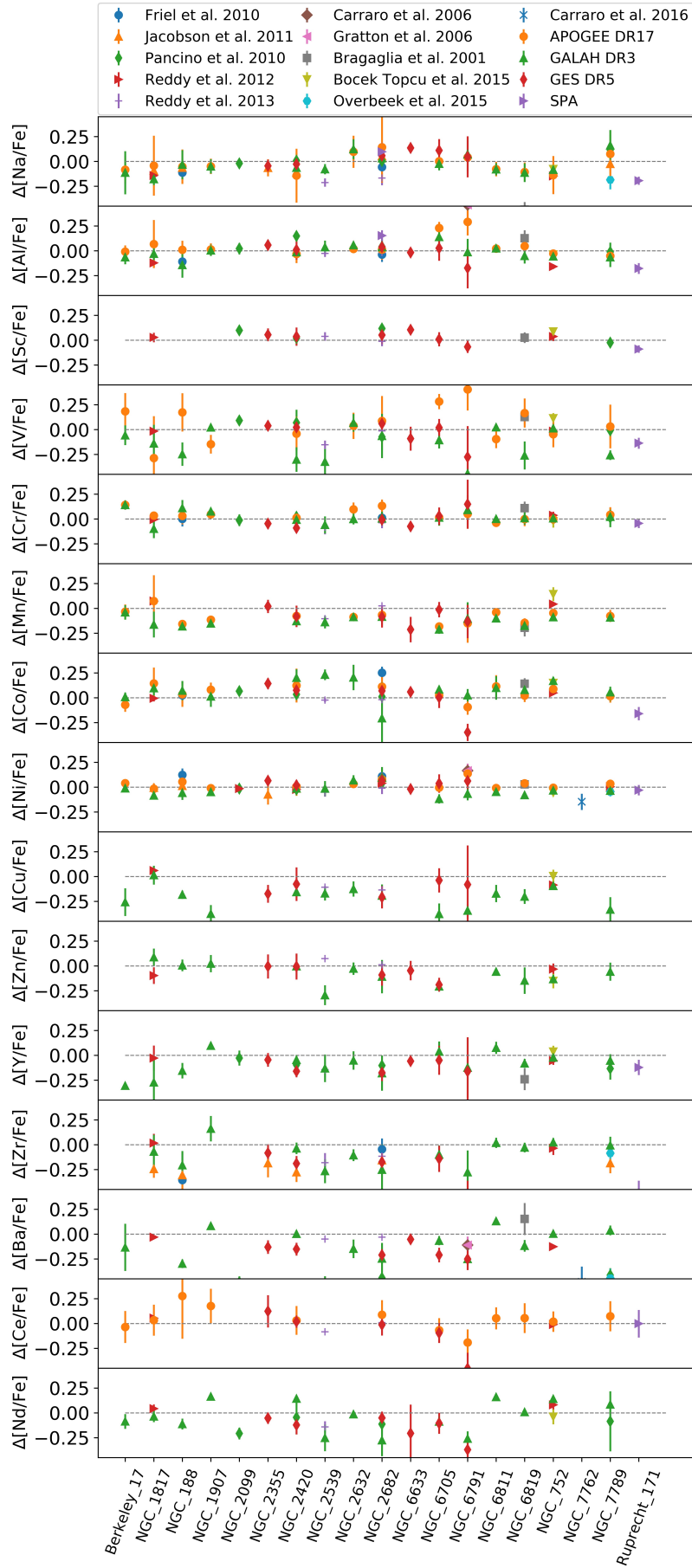


Fig. A.3. Comparison of the abundances for OCs in common with high-resolution ($R > 20000$) spectroscopic studies (this work-literature) for elements not shown in Fig. 8.